



SIA

Project Title:	System for vehicle-infrastructure Interaction Assets health status monitoring
Starting date:	01/03/2018
Duration in months:	36
Call (part) identifier:	H2020-GALILEO-GSA-2017-1
Grant agreement no:	776402

Deliverable D5.4: Linking of Physical Parameters with Component Health Status

Due date of deliverable	Month 27
Actual submission date	30-07-2021
Organization name of lead contractor for this deliverable	VIAS
Dissemination level	PU
Revision	5.0

Authors

Author(s)	CEIT Borja Rodríguez Blas Blanco Imanol Puy Unai Alvarado
Contributor(s)	DLR Benjamin Baasch Judith Heusel Thorsten Neumann VIAS Manuel Menéndez FGC Paula Ciria Espinosa

HISTORY OF CHANGES		
Version	Publication date	Change
1.0	1/6/2020	▪ Document draft finalization and creation of v1.0
2.0	4/6/2020	▪ Integration of feedback from TEL
3.0	11/06/2020	▪ Integration of review by ING and NSL
4.0	14/07/2020	▪ Integration of comments in DRS (27/06/2020)
5.0	26/07/2021	▪ Integration of comments in DRS (18/07/2020)

Executive Summary

SIA (System for vehicle-infrastructure Interaction Assets health status monitoring) has the objective of developing four ready-to-use new services to provide prognostic information about the health status of the railway's most demanding assets in terms of maintenance costs, at the points of the interaction between the vehicle and the infrastructure (wheelset, pantograph, rail and catenary, i.e. iCatMon, iPantMon, iWheelMon and iRailMon respectively).

Deliverable D2.1 compiled a detailed set of failure modes and degradation mechanisms related to the assets relevant to SIA, as well as the associated maintenance actions. These use cases establish a set of KPIs that provide information about the health status of the assets mentioned above:

- **Use case #1:** contact wire wear
- **Use case #2:** contact wire incorrect height & stagger
- **Use case #3:** contact strip normal wear (normal / asymmetric)
- **Use case #4:** wheel flats and polygonization wear
- **Use case #5:** Rail corrugations
- **Use case #6:** Short-wave irregularities

This document presents the linking of the physical parameters that are measured by the onboard equipment with the health status of the different assets. To that, the following information is provided:

- A description of the different KPIs
- The input information that is necessary to derive the different KPIs (e.g. physical signals, mathematical models, etc.)
- The methodology derived for health assessment.

This information is common to all the use cases, which has been presented as a function of the high-level application they are related to:

- iCatMon related information is described in chapter 2
- iPantMon related information is described in chapter 3
- iWheelMon related information is described in chapter 4
- iRailMon related information is described in chapter 5

Table of Contents

EXECUTIVE SUMMARY	3
TABLE OF CONTENTS	4
ABBREVIATIONS AND ACRONYMS.....	8
1 INTRODUCTION.....	10
1.1 SIA PROJECT	10
1.2 DEFINITION OF USE CASES	11
1.3 HEALTH ASSESSMENT	12
2 ICATMON HEALTH STATUS ASSESSMENT.....	13
2.1 DESCRIPTION OF ICATMON HEALTH-RELATED KPIS ACCORDING TO THE USE CASES.....	13
2.1.1 <i>Overhead Contact Wire Wear</i>	13
2.1.2 <i>Overhead Contact Wire Height</i>	13
2.1.3 <i>Overhead Contact Wire Stagger</i>	14
2.1.4 <i>Pantograph-Catenary Interaction</i>	14
2.2 DESCRIPTION OF INPUTS	16
2.2.1 <i>Physical Parameters</i>	16
2.2.2 <i>Measured Signals</i>	16
2.3 DESCRIPTION OF HEALTH ASSESSMENT METHODOLOGY	17
2.3.1 <i>Pantograph-Catenary Interaction Assessment</i>	17
3 IPANTMON HEALTH STATUS ASSESSMENT	40
3.1 DESCRIPTION OF IPANTMON HEALTH-RELATED KPIS ACCORDING TO THE USE CASES.....	40
3.1.1 <i>Wear Of Contact Strips</i>	40
3.1.2 <i>Pantograph-Catenary Interaction</i>	40
3.2 DESCRIPTION OF INPUTS.....	40
3.3 DESCRIPTION OF HEALTH ASSESSMENT METHODOLOGY	40
3.3.1 <i>Pantograph-Catenary Interaction Assessment</i>	40
3.3.2 <i>Estimation Of The Contact Strip Wear</i>	41
4 IWHEELMON HEALTH STATUS ASSESSMENT	42
4.1 DESCRIPTION OF IWHEELMON HEALTH-RELATED KPIS ACCORDING TO THE USE CASES	42
4.1.1 <i>Wheel Flats</i>	42
4.1.2 <i>Polygonization Wear</i>	42
4.2 DESCRIPTION OF INPUTS.....	44
4.2.1 <i>Physical Parameters</i>	44
4.2.2 <i>Measured Signals</i>	45
4.3 DESCRIPTION OF HEALTH ASSESSMENT METHODOLOGY	45
4.4 RESULTS AND CONCLUSIONS.....	47
4.4.1 <i>The Impact of E-GNSS</i>	48
5 IRAILMON HEALTH STATUS ASSESSMENT	50

5.1	DESCRIPTION OF IRAILMON HEALTH-RELATED KPIS ACCORDING TO THE USE CASES.....	50
5.1.1	<i>Rail Corrugation</i>	50
5.1.2	<i>Short-wave Irregularities</i>	51
5.2	DESCRIPTION OF INPUTS.....	53
5.2.1	<i>Physical Parameters</i>	53
5.2.2	<i>Measured Signals</i>	54
5.3	DESCRIPTION OF HEALTH ASSESSMENT METHODOLOGY	54
5.4	RESULTS AND CONCLUSIONS	55
5.4.1	<i>The Impact of E-GNSS</i>	59
6	REFERENCES.....	60

LIST OF FIGURES

FIGURE 1. EXAMPLE OF INFORMATION PROVIDED BY <i>iRAILMon</i> TO THE INFRASTRUCTURE MANAGER	11
FIGURE 2. (A) FGC REAL PANTOGRAPH. (B) SKETCH OF THE THEORETICAL MODEL	17
FIGURE 3. (A) PANHEAD HEIGHT AGAINST LOWER ARM ANGLE. (B) PANHEAD TRAJECTORY	18
FIGURE 4. (A) SKETCH OF FGC MECHANISM (B) KINEMATIC ASSESSMENT OF THE MECHANISM FOR APPLIED TORQUE	19
FIGURE 5. (A) SPRINGS DEFORMATION. (B) SPRINGS DISTANCE	19
FIGURE 6. APPLIED TORQUE TO THE LOWER ARM	20
FIGURE 7. SKETCH FOR STRUCTURE STATIC FORCE CALCULATION	20
FIGURE 8. APPLIED TORQUE ON THE LOWER ARM. FROM MEASURED FORCE (BLUE). FROM KINEMATICAL ASSESSMENT (RED)	21
FIGURE 9. SKETCH FROM STRUCTURE TO LUMPED MASS	22
FIGURE 10. DIFFERENT DYNAMIC RESPONSE AS A FUNCTION OF THE PANHEAD'S HEIGHT	22
FIGURE 11. BASIC SCHEME OF A DOUBLE CONTACT WIRE CATENARY	24
FIGURE 12 (A) FRONT AND LATERAL VIEWS OF THE LUMPED MASS MODEL OF THE PANTOGRAPH. (B) SCHEME OF THE PANTOGRAPH COLLECTOR IMPLEMENTED DESIGN. (C) NORMALIZED SHAPE FUNCTIONS OF THE PANTOGRAPH COLLECTOR	26
FIGURE 13. PREDICTED FREQUENCY RESPONSE FUNCTIONS OF THE PANTOGRAPH COLLECTOR WHEN THEY ARE INSTALLED AND FREELY SUSPENDED. SOLID LINE: PANTOGRAPH COLLECTOR INSTALLED ON THE STRUCTURE. DASHED: PANTOGRAPH COLLECTOR FREELY SUSPENDED	27
FIGURE 14. THE INITIAL POSITION FOR THE CATENARY TYPE CA-220. ONE CONTACT WIRE (LEFT) AND TWO CONTACT WIRES (RIGHT). NO UNCERTAINTIES ARE INTRODUCED	29
FIGURE 15. THE INITIAL POSITION FOR THE CATENARY TYPE CA-220 CONSIDERING UNCERTAINTIES. ONE CONTACT WIRE (LEFT) AND TWO CONTACT WIRES (RIGHT). RANDOMNESS: $\Sigma S = 2$ CM AND $\Sigma D = 6.6$ MM	29
FIGURE 16. TIME-DOMAIN RESULTS OF PANTOGRAPH CATENARY INTERACTION WITH THE PARAMETERS SET ACCORDING TO EN 50318	32
FIGURE 17. POWER SPECTRAL DENSITY OF THE CONTACT FORCES FOR DIFFERENT NUMBER OF ELEMENT MODELLING THE WIRE WITHIN ADJACENT DROPPERS	32
FIGURE 18. RATIO BETWEEN THE STANDARD DEVIATIONS OF COLLECTOR ACCELERATIONS AND THE CONTACT FORCE. (A) REAR COLLECTOR. LOW-PASS FILTER 20 Hz. (B) REAR COLLECTOR. HIGH-PASS FILTER 20 Hz. (C) FRONT COLLECTOR. LOW-PASS FILTER 20 Hz. (D) FRONT COLLECTOR. HIGH-PASS FILTER 20 Hz.	33
FIGURE 19. PREDICTED CONTACT FORCE, ELECTRICAL RESISTANCE, CURRENT INTENSITY AND NWR FOR A VEHICLE TRAVELLING AT 200 KM/H, 1000 A AS THE TOTAL INTENSITY DEMANDED BY THE VEHICLE AND LEVEL 2 OF UNCERTAINTIES	36
FIGURE 20. ESTIMATION OF THE MEAN WIRE WEAR ON THE FIRST CONTACT WIRE (LEFT) AND ACCURACY OF THE REGRESSION MODEL (RIGHT)	37
FIGURE 21. ESTIMATION OF THE MEAN WIRE WEAR ON THE SECOND CONTACT WIRE (LEFT) AND ACCURACY OF THE REGRESSION MODEL (RIGHT)	37
FIGURE 22. ESTIMATION OF THE RATIO BETWEEN MAXIMUM AND MEAN WEAR OF THE CONTACT WIRES (LEFT) AND THE ACCURACY OF THE ESTIMATION	38
FIGURE 23. DISTANCE FROM RAIL SURFACE TO CONTACT WIRE	38
FIGURE 24. CHANGE OF THE VALUE OF THE NATURAL FREQUENCIES OF THE COLLECTOR AS THE GRAPHITE IS WORN	41
FIGURE 25. POLYGONIZATION WEAR OF A SOLID STEEL WHEEL WITH THREE DOMINANT HARMONICS AROUND THE WHEEL CIRCUMFERENCE. THE BARS INDICATE THE DISTRIBUTION OF DIFFERENT HARMONICS. (TAKEN FROM [5].)	43
FIGURE 26. PERMITTED DEVIATION FROM ROUNDNESS ACCORDING TO ANNEX I OF EN15313 [7].	44
FIGURE 27. CEPSTRUM ANALYSIS OF A PERIODIC EXCITATION CAUSED BY A WHEEL FLAT.	45
FIGURE 28. POWER CEPSTRUM IN THE FREQUENCY DOMAIN FROM 1 TO 15 M OF AXLE BOX ACCELERATION DATA AT AN AVERAGE WINDOW SPEED OF 27.34 M/S. DIFFERENT COLOURS REPRESENT THE POWER CEPSTRA OF THE DIFFERENT WINDOWS OF APPROXIMATELY 13 SECONDS OF DATA	47

FIGURE 29. POWER CEPSTRUM IN THE QUEFREQUENCY DOMAIN 1 TO 15 M OF AXLE BOX ACCELERATION DATA AT AN AVERAGE WINDOW SPEED OF 13.04 M/S.	48
FIGURE 30. EXAMPLE OF SHORT-PITCH CORRUGATION.	50
FIGURE 31. EXAMPLES OF SQUATS ON THE RUNNING SURFACE OF THE RAILHEAD.	52
FIGURE 32. ABA DATA PROCESSING SEQUENCE TO EXTRACT CHARACTERISTIC FEATURES FOR THE RAIL HEALTH STATUS ASSESSMENT.	55
FIGURE 33. RAW ABA DATA IN THE TIME DOMAIN (GREY) AND GNSS SPEED (BLUE).	56
FIGURE 34. TIME-FREQUENCY REPRESENTATION OF RAW ABA DATA.	57
FIGURE 35. RMS FEATURES FROM EIGHT DIFFERENT WAVENUMBER BANDS.	58

LIST OF TABLES

TABLE 1 RANGES DEFINED BY THE STANDARD EN 50318 AND RESULTS OBTAINED WITH THE MODEL.....	32
--	----

Abbreviations and Acronyms

Abbreviation / Acronyms & relevant definitions	Description
ABA	Axlebox Acceleration
AHC	Anti Headcheck
CBM	Condition Based Maintenance
DC	Direct current
DOC	Dilution of precision
DOF	Degree of Freedom
EGNSS	European Global Navigation Satellite Systems
FE	Finite Elements
FGC	Ferrocarrils de la Generalitat de Catalunya. Spanish regional train operator
GNSS	Global Navigation Satellite System
GSA	European Global Navigation Satellite Systems Agency
iCatMon	The application that provides information about the status of the catenary
iPantMon	The application that provides information about the status of the pantograph
iRailMon	The application that provides information about the status of the rail
iWheelMon	The application that provides information about the status of the wheelset
IM	Infrastructure Manager
IO	Integrated Operator
KP	Kilometric Point
KPI	Key Performance Indicator
LCC	Life Cycle Cost
NWR	Normalized Wear Rate
ÖBB	Österreichische Bundesbahnen- Austrian Federal Railways, a national train operator
OCL	Overhead Contact Line
OCW	Overhead Contact Wire
OOR	Out of Round
RCF	Rolling Contact Fatigue
RMS	Root Mean Square
STFT	Short-Time Fourier Transform

SIA	System for vehicle-infrastructure Interaction Assets health status monitoring
SIA_ABA	SIA subsystem: an onboard device that senses the wheelset-rail interaction
SIA_DH	SIA subsystem: an onboard device that integrates the data coming from onboard sensors (SIA_ABA and SIA_PANT), synchronizes the data with time & position (SIA_POS), stores it and sends it to the visualization platform (SIA_VP)
SIA_PANT	SIA subsystem: an onboard device that senses the pantograph-catenary interaction
SIA_POS	SIA subsystem: an onboard device that calculates the position of the train to synchronize it with the signals of the sensors
SIA_VP	SIA subsystem: back-office applications that analyze and visualize the data within iCatMon, iPantMon, iWheelMon and iRailMon applications
SW	Software
TOC	Train Operating Company

1 Introduction

1.1 SIA project

SIA (System for vehicle-infrastructure Interaction Assets health status monitoring) has the objective of developing four ready-to-use new services to provide prognostic information about the health status of the railway's most demanding assets in terms of maintenance costs, at the points of the interaction between the vehicle and the infrastructure (wheelset, pantograph, rail and catenary). More specifically, the common features of the new services (iWheelMon, iPantMon, iRailMon and iCatMon) are detailed below:

1. Plug-in software based Web Application to be integrated with already existing maintenance information systems, avoiding the need to replace the entire system.
2. Real-time information about assets health status and views of prognostic health status with different time frames to make projections of future scenarios (e.g. future maintenance costs, remaining useful life of the rail and estimated necessary investment).
3. A gateway to maintenance workflow managing software which can trigger maintenance actions and inform traffic management information systems about early detected failures in components that can trigger speed restrictions or line blocking.

In addition, the specific characteristics of the new four services are highlighted below:

- iWheelMon, which is intended for TOCs (Train Operating Companies) and IOs (Integrated Operators), will provide real-time information about the status of the wheel (e.g. presence of wheel flats) and prognostic health status information within a certain time frame such as predicted wear, RCF and polygonization, and maintenance recommendations for meeting ISO 1005-8 [1] and TOC specific requirements.
- iPantMon, which is intended for TOCs and integrated operators, will provide real-time information about the status of the pantograph (e.g. incorrect vertical damping forces of the upper arm) and prognostic health status information in a certain time frame such as wearing of contact stripes, and maintenance recommendations for meeting EN 50405 [2] and TOC specific requirements.
- iRailMon, which is intended for IMs and maintenance subcontractors, will provide real-time information about the status of the rail and prognostic health status information in a certain time frame such as squats, corrugation, wear and RCF, and maintenance recommendations according to IM specific maintenance requirements.
- iCatMon which is intended for IMs and maintenance subcontractors, will provide real-time information about the status of the catenary (e.g wearing of cable) and prognostic health status information in a certain time frame such as the inclination of the mooring balance with respect to the rail, break of the automatic regulation pulley, wear of cables, and maintenance recommendations for meeting EN50119 [3].

Figure 1 illustrates one example of the new information that iRailMon will provide to the infrastructure manager.

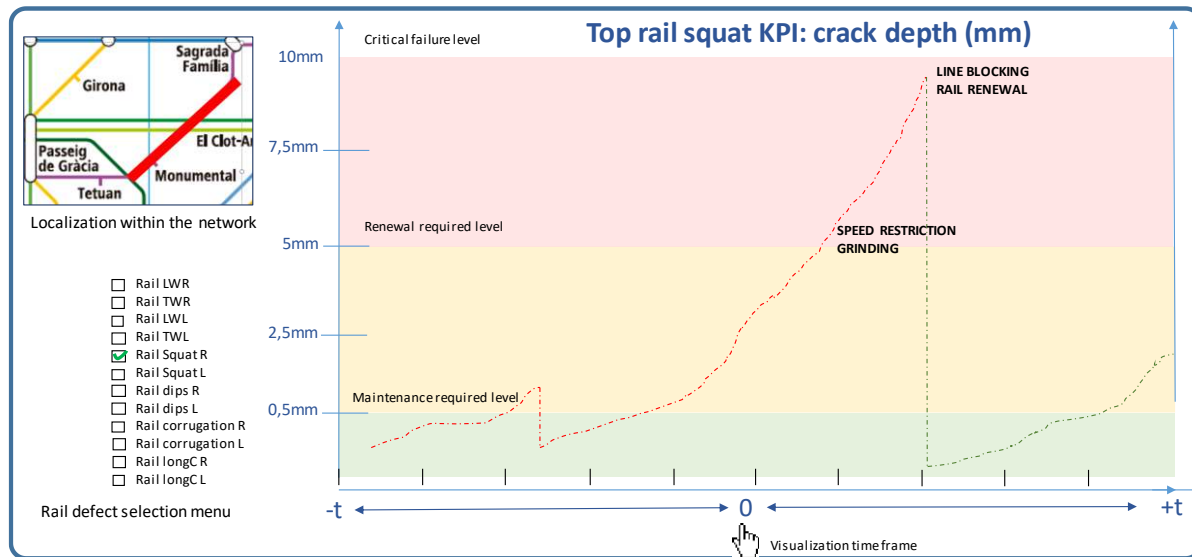


Figure 1. Example of information provided by *iRailMon* to the infrastructure manager

1.2 Definition of Use Cases

Deliverable D2.1 [4] compiled a detailed set of failure modes and degradation mechanisms related to the assets relevant to SIA, as well as the associated maintenance actions. This set of failure modes implies many different means of detection and handling of information. Therefore, it is not feasible to tackle them all by the system and applications to be developed within SIA.

For that reason, a set of use cases were selected in terms of

- Their impact on the operations and frequency of appearance
- The technical feasibility of their detection by means of low-cost sensors
- The feasibility of predicting the evolution of the damage in terms of physical modelling
- The interests and feedback from end-users of the consortium

This is the list of use cases that are relevant for the project:

- **iCatMon.** The contact wire is the main component of an overhead contact line. Its main function is to ensure current transmission to the train through sliding contact within pantograph strips. It is subject to two main failure modes: bad positioning and important wear. Additionally, the contact wear overhaul is the most expensive cost of the overhead contact line maintenance budget. For that reason, the two use-cases dedicated to iCatMon will tackle these failure mechanisms.
 - **Use case #1:** contact wire wear
 - **Use case #2:** contact wire incorrect height & stagger
- **iPantMon.** The interaction between the pantograph and OCL takes place between the OCW and the pantograph's contact strips. Failures associated to contact strips account for more than 75% of defects in the pantograph. Currently at FGC, the means of inspection to

detect wear on the contact strips is based on visual inspection when the train enters the workshop. A degraded pantograph (i.e.: with a damaged contact strip) has a direct impact on the wear pattern of the OCW which, as said above, is the the most important component of the catenary. Therefore, this failure mechanism will be tackled as use case within the project.

- **Use case #3:** contact strip normal wear (normal / asymmetric)
- **iWheelMon.** Out-of-roundness defects on the wheelset are the most important of this component, due to two important reasons. On the one hand, polygonization defects could seriously compromise the safety of operation by increasing the probability of derailment. On the other hand, they can seriously damage the track quality. Wheel flats may have a critical importance in the track geometry degradation, which accounts for the greatest costs in terms of maintenance. A way of predicting these defects could potentially benefit the leverage of CBM mechanisms to address track access charges by IMs to TOCs.
 - **Use case #4:** wheel flats and polygonization wear
- **iRailMon.** In addition to track geometry-related defects, those on the rail account for the gratest contribution in the LCC of railway infrastructure. Among the failure mechanisms described in D2.1 [4], rail corrugations and short-wave irregularities have the greatest impact on noise emissions and safety. For these reasons, the following use cases will be tackled by the project.
 - **Use case #5:** Rail corrugations
 - **Use case #6:** Short-wave irregularities

1.3 Health Assessment

One of the main goals of the project is to assess the health of some of the most relevant assets of the railway system (i.e. catenary, pantograph, wheelset and rail) in the form of KPIs, according to the use cases defined above.

For that purpose, a set of onboard systems have been developed (deliverables D4.1 [5] and D4.3 [6]), in charge of measuring physical signals and transmit them to the back-office applications, so these physical signals can be transformed into the correspondent KPIs.

- SIA_ABA subsystem is in charge of measuring the required physical signals to assess the wheel-rail interaction.
- SIA_PANT subsystem is in charge of measuring the required physical signals to assess the pantograph-catenary interaction.

The methodologies and algorithms that transform these physical signals into the relevant methodologies is described in this document, that constitutes one of the most scientifically-relevant activities of the SIA project.

2 iCatMon Health Status Assessment

2.1 Description of iCatMon Health-Related KPIs According To The Use Cases

According to the definition of use cases of deliverable D2.1, those related to the health status assessment of the OCW (iCatMon application) are

- Use case #1: contact wire wear
- Use case #2: contact wire incorrect height & stagger

Also, KPIs related to the interaction of the pantograph-catenary system will be described:

- Contact force
- Vertical displacement of a contact point
- Shocks

2.1.1 Overhead Contact Wire Wear

The interaction between pantograph and catenary progressively damages the contact surfaces due to three wear mechanisms; mechanical, electrical and arc wear. The mechanical wear is due to the sliding of the pantograph contact strip over the contact wire while exerting a certain pressure to maintain a constant contact between both surfaces. The electrical wear is caused by the heating of surfaces due to the flow of electrical current between pantograph and catenary along with the electrical resistance between contact surfaces. Finally, the arc wear is due to the separation of contact surfaces that causes electric arcs that lead to a sudden increase in temperature with the subsequent loss of material. The total wear of the contact wire is due to the contribution of each one of these mechanisms, which are in turn related within themselves.

This KPI is expressed in terms of the Normalized Wear Rate (NWR) [mm^3/km], and it is visualized in iCatMon in these two ways:

- a) Spatial wear: wear [mm^3/km] vs distance [KP – m]. This KPI assesses the OCW wear as a function of the distance (KP) of the line, according to:
 - a. Instant wear, i.e. a single travel
 - b. Maximum, minimum, average & standard deviation, of the OCW wear for more than a single journey, given a period of time.
- b) Wear over time: wear [mm^3/km] vs time [days]. This KPI assesses the OCW wear as a function of time (days) at a given location (KP) of the line, according to:
 - a. Maximum, minimum, average & standard deviation

2.1.2 Overhead Contact Wire Height

This KPI measures the relative height between the track and OCW. The height of the OCW with respect to the track's rolling plane has a nominal design value which changes dynamically due to the uplifting force exerted by the sliding pantograph. The knowledge of this force is therefore very important to evaluate the expected uplift value and the consequent difference between dynamic

and static values. The height value is checked against a threshold value defined by standards that allow the trains to reach the desired speed.

This KPI is expressed in [mm], and it is visualized in iCatMon in these two forms:

- a) Height over longitudinal displacement: height [mm] vs distance [KP – m]. This KPI assesses the OCW height as a function of the distance (KP) of the line, according to:
 - a. Instant height, i.e. a single travel
 - b. Maximum, minimum, average & standard deviation, of the OCW height for more than a single travel, given a period of time
- b) Height over time: height [mm] vs time [days]. This KPI assess the OCW height as a function of time (days) at a given location (KP) of the line, according to:
 - a. Maximum, minimum, average & standard deviation

2.1.3 Overhead Contact Wire Stagger

The stagger of the OCW is given by the distance between the track axis and the middle line of the pantograph's contact strip. The stagger shall not exceed a limit value defined during the design in order to avoid pantograph dewirement and cross-wind effects.

This KPI is expressed in [mm], and it is visualized in iCatMon in these two forms:

- a) Spatial stagger: stagger [mm] vs distance [KP – m]. This KPI assesses the OCW stagger as a function of the distance (KP) of the line, according to:
 - a. Instant stagger, i.e. a single travel
 - b. Maximum, minimum, average & standard deviation, of the OCW stagger for more than a single travel, given a period of time
- b) Stagger over time: stagger [mm] vs time [days]. This KPI assess the OCW height as a function of time (days) at a given location (KP) of the line, according to:
 - a. Maximum, minimum, average & standard deviation

2.1.4 Pantograph-Catenary Interaction

Apart from the geometrical KPIs (wear, height and stagger) that are commonly provided by measurement trains, iCatMon manages a set of KPIs that are referred to the OCW dynamic behaviour as a consequence of its interaction with the pantograph. These KPIs are described in the following subsections.

2.1.4.1 Contact Force

The pantograph gently pushes the OCW wires with an uplift force to achieve a uniform electrical contact. If this force is too loose, the contact might be lost and both electric arcs and traction inefficiencies may arise. On the contrary, if the force is too tight, the wear of both OCW and contact strips is accelerated.

This KPI is expressed in [N], and it is visualized in iCatMon in these two forms:

- a) Spatial contact force: contact force [N] vs distance [KP – m]. This KPI assesses the contact force as a function of the distance (KP) of the line, according to:
 - a. Instant contact force, i.e. a single travel
 - b. Maximum, minimum, average & standard deviation, of the contact force for more than a single travel, given a period of time
- b) Contact force over time: contact force [N] vs time [days]. This KPI assess the contact force as a function of time (days) at a given location (KP) of the line, according to:
 - a. Maximum, minimum, average & standard deviation

2.1.4.2 Vertical displacement of contact point

This KPI assesses the height correspondent to the vertical displacement of the contact point between the pantograph and OCW as a consequence of the uplift force. It is related to the OCW height described in 2.1.2.

This KPI is expressed in [mm], and it is visualized in iCatMon in these two forms:

- a) Spatial height: height [mm] vs distance [KP – m]. This KPI assesses the OCW height as a function of the distance (KP) of the line, according to:
 - a. Instant height, i.e. a single travel
 - b. Maximum, minimum, average & standard deviation, of the OCW height for more than a single travel, given a period of time
- b) Height over time: height [mm] vs time [days]. This KPI assess the OCW height as a function of time (days) at a given location (KP) of the line, according to:
 - a. Maximum, minimum, average & standard deviation

2.1.4.3 Shocks

Apart from the KPIs described above, the interaction between the pantograph and the catenary may suffer from isolated events (e.g. hard spots in the OCW, small objects and even pantograph's dewirement) that lead to discrete shocks.

A simple KPI accounting for shocks is visualized in iCatMon, in the form of

- Shock category (i.e. 1, 2, 3, 4) according to its impact in the pantograph's dynamics, concerning the severity of the event leading to the shock
- Location of the shock (coordinates and KP)
- The recurrence that assesses whether the shock occurs at every passage
- The evolution of the shock that evaluates whether the shock is becoming more detrimental

2.2 Description Of Inputs

The KPIs exposed above cannot be measured directly unless invasive either expensive measurement devices are employed. Nevertheless, they can be pointed out through other physical parameters, which are more easily obtained, and interpreted with the aid of physical models that reproduce to a certain extent the reality.

2.2.1 Physical Parameters

The physical parameters used to assess the KPIs are:

- Speed of the train
- Pantograph collector accelerations (measured signal, section 2.2.2)
- Movement of pantograph's lower arm (measured signal, section 2.2.2)
- Mean nominal force (obtained when servicing the pantograph at the workshop)
- Slope of the route
- Efficiency of the traction equipment
- Vehicle mass
- Pantograph model (section 2.3.1.1)
- Catenary model (2.3.1.2)

2.2.2 Measured Signals

2.2.2.1 Signal 1: Lower Arm Angle

The kinematical assessment of the pantograph's main structure shows that the position of any part can be known using the position of another part.

Displacement sensors are not suitable for large displacement in the case of a pantograph which is subjected to a complex environment. Laser-based solutions are quite complicated to install and expensive.

Monitoring of the lower arm angle only needs of an inclinometer assembled to the bar. The measurement range must be at least ± 30 degrees to cover extreme positions. This signal is measured close to the base frame avoiding the wiring of the pantograph.

2.2.2.2 Signal 2: Panhead Acceleration 1 And 2

As shown in previous sections the acceleration signals can give an insight into the contact force, the irregularities of the contact wire and the wear of pantograph collector. The acceleration will be measured in both strips of the pantograph. The maximum absolute value is expected to be below 5 g.

2.3 Description Of Health Assessment Methodology

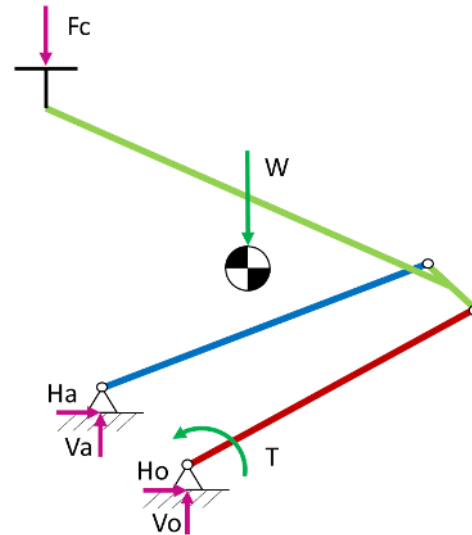
2.3.1 Pantograph-Catenary Interaction Assessment

2.3.1.1 Pantograph Model

Several calculations have been carried out to assess the physical parameters of the pantograph model. These calculations aim to obtain a representative theoretical model from the real pantographs that are going to operate.



(a)



(b)

Figure 2. (a) FGC Real pantograph. (b) Sketch of the theoretical model

A pantograph can be split into the main structure and panhead. Both parts are linked through an upper-joint, which give at least one vertical degree of freedom (DOF).

The main structure is a one DOF mechanism, controlled by a torque applied in one of its bars attached to the base frame. The bar where the torque is applied is the so-called lower arm. This torque (T) allow for the equilibrium between the whole weight of the pantograph (W) and the contact force (F_c).

2.3.1.1.1 Kinematic Assessment

Firstly, the kinematic assessment of pantograph's structure is carried out to obtain the relationship between the positions of different parts. The following figure shows the position of the panhead's top side regarding base frame bottom side against the tilting of the lower arm. The same assessment gives the trajectory of the panhead.

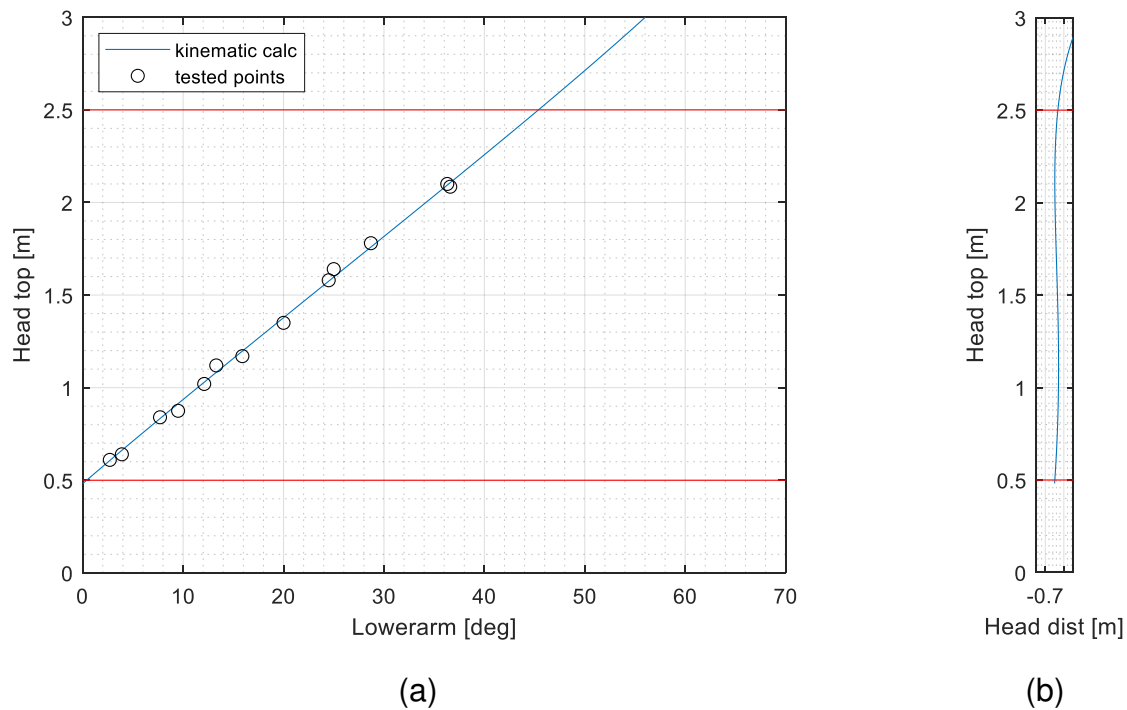


Figure 3. (a) Panhead height against lower arm angle. (b) Panhead trajectory

2.3.1.1.2 Static Contact Force

The static contact force is related to the torque applied between the base frame and the lower arm. If masses, centres of gravity of different parts and one of these two parameters are known the other one could be obtained.

This assumption has been checked through two procedures with the FGC pantograph:

- 1 Calculation of applied torque by FGC pantograph's mechanism:

FGC pantograph has two identical mechanisms at each side. These are a one DOF mechanisms attached to the lower arm and controlled by the deformation of a linear coil spring. The deformation of coil springs δ_s and their distance d_s to the reference point apply a torque T according to stiffness value of coil springs K_s .

$$T(\theta) = K_\theta \cdot \theta = F_s \cdot d_s = K_s \cdot \delta_s \cdot d_s \quad (1)$$

These mechanisms are adjusted at depot with the target of support a known load at different positions of panhead's trajectory. For the adjustment, the initial deformation of springs is set and its trajectory is controlled with two bolts on each side of the lower arm.

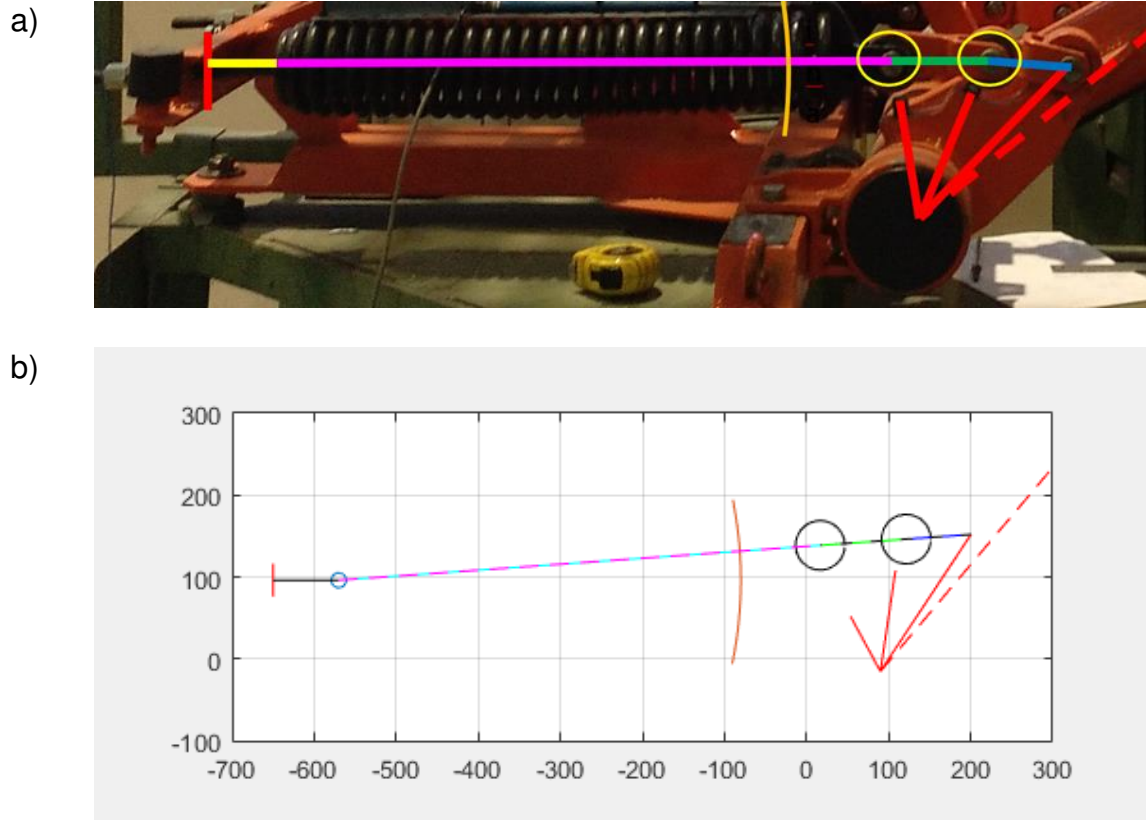


Figure 4. (a) Sketch of FGC mechanism (b) Kinematic assessment of the mechanism for applied torque

From the kinematic assessment of each mechanism: the deformation of springs δ_s and their distance d_s to the reference point is obtained.

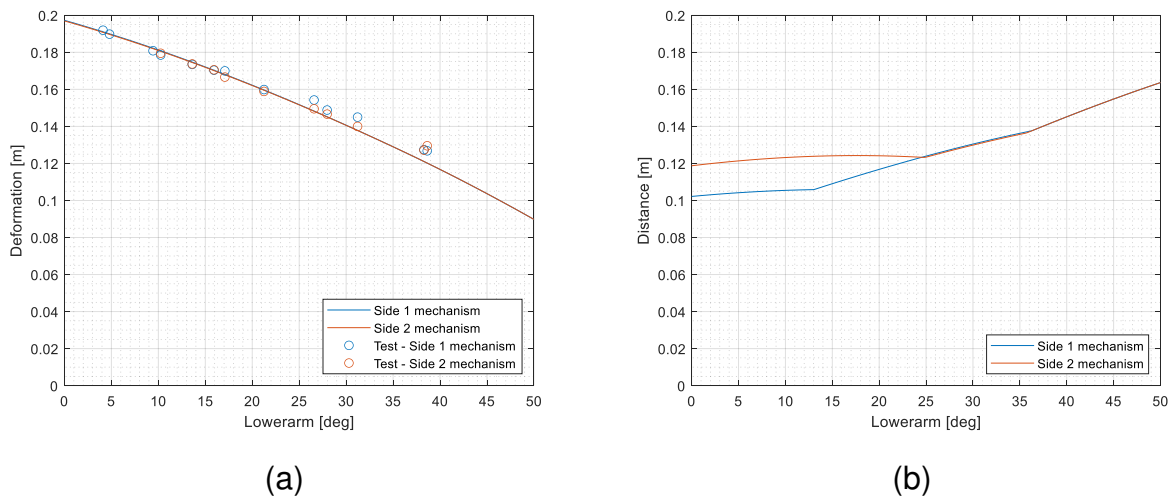


Figure 5. (a) Springs deformation. (b) Springs distance

The total applied torque is the sum of both mechanisms:

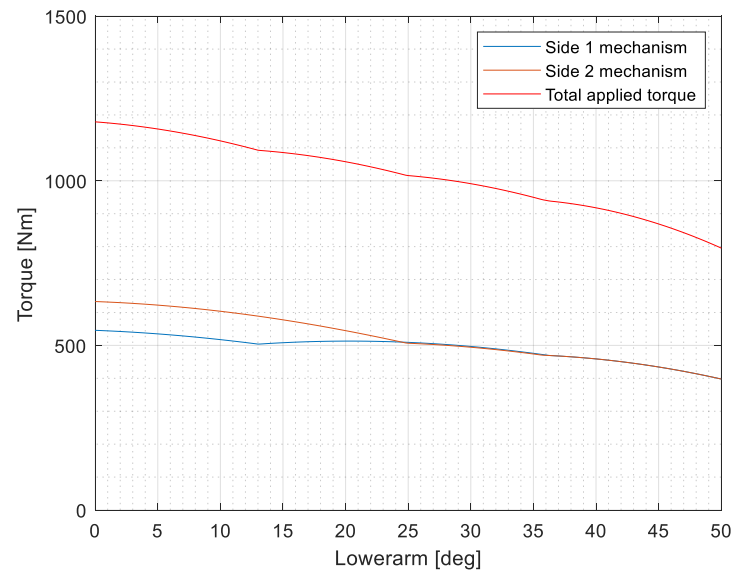


Figure 6. Applied torque to the lower arm

2 Calculation of the required torque when a known contact force is applied:

The pantograph is a hyperstatic structure where contact force, whole weight and the torque applied are at equilibrium. This problem can be solved cutting the structure on the points with articulated joints.

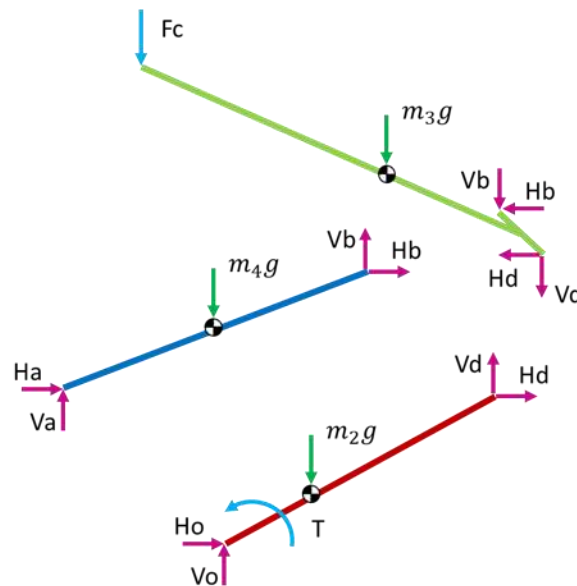


Figure 7. Sketch for structure static force calculation

If the 9 equations and 9 variables system is solved for a tested contact force value, the applied torque is obtained. This value is quite similar to the obtained in the assessment of FGC pantograph mechanism

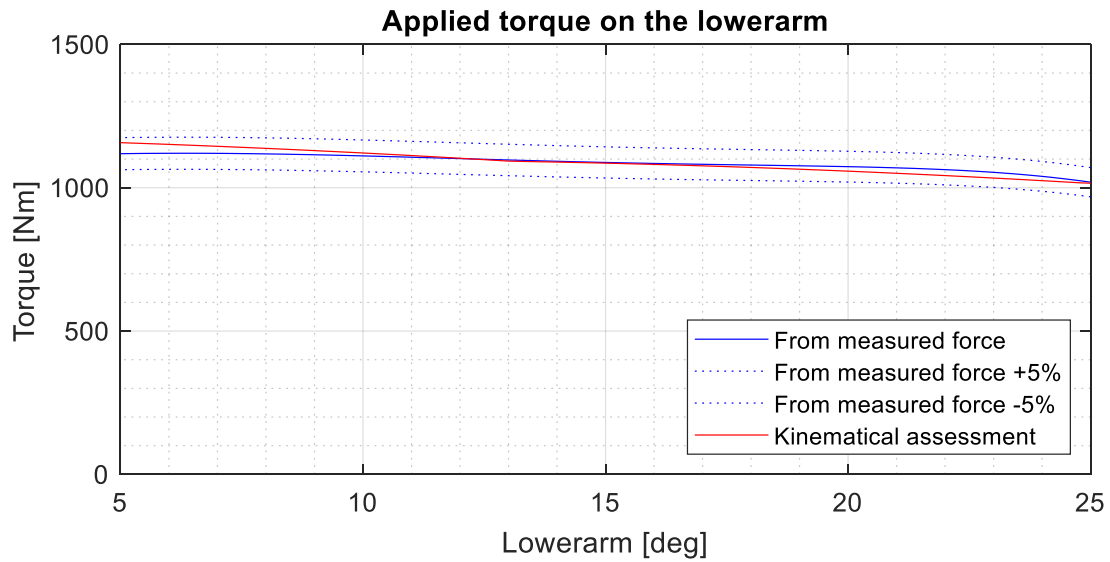


Figure 8. Applied torque on the lower arm. From measured force (blue). From kinematical assessment (red)

2.3.1.1.3 Dynamic Model

The validation of the above calculations regarding tested values allows converting a real pantograph to a simplified model, which could be used along with pantograph-catenary interaction models.

Using Lagrange and movement equations is possible to convert the pantograph structure in a lumped mass system.

$$\frac{d}{dt} \left(\frac{\partial L}{\partial \dot{q}_i} \right) - \frac{\partial L}{\partial q_i} = Q_i \quad (2)$$

$$\begin{bmatrix} [M] & 0 \\ 0 & [M] \end{bmatrix} \begin{bmatrix} \{\ddot{z}\} \\ \{\dot{z}\} \end{bmatrix} + \begin{bmatrix} [c] & [k] \\ [-M] & 0 \end{bmatrix} \begin{bmatrix} \{\dot{z}\} \\ \{z\} \end{bmatrix} = \begin{bmatrix} \{f\} \\ 0 \end{bmatrix} \quad (3)$$

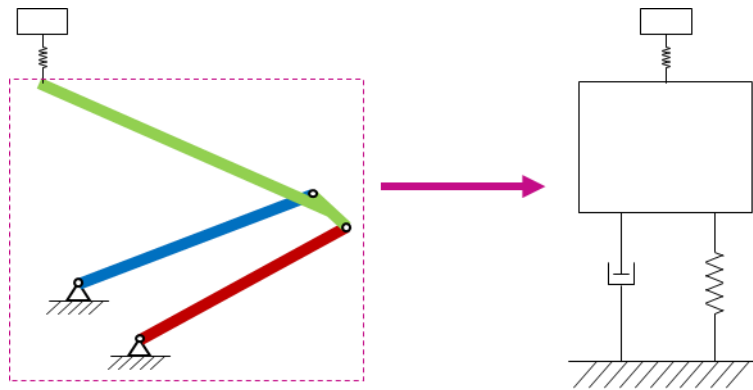


Figure 9. Sketch from structure to lumped mass

The mass, stiffness and damping values will depend on the position of the pantograph given different dynamic responses:

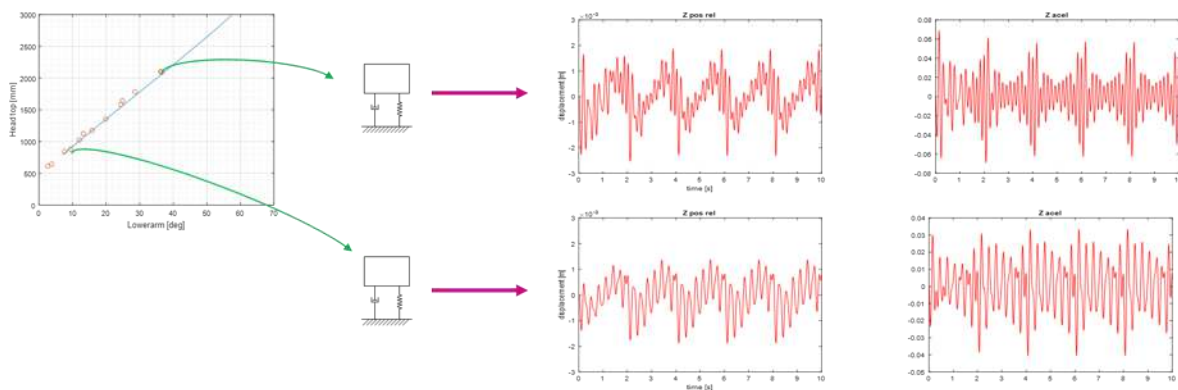


Figure 10. Different dynamic response as a function of the panhead's height

2.3.1.2 Catenary Model

The catenary structure has several features that make it a difficult system to be modelled and solved straightforwardly. Some of these features are:

- Large size in its longitudinal dimension: A model of catenary should be long enough to reproduce realistically the dynamic behaviour between tensioning positions. This fact involves the use of large models that reduce the computational efficiency of the conventional numerical methods.
- Initial static position: Due to its large flexibility the initial vertical position of the catenary mainly depends on its weight, the tensioning and the length of droppers.
- Non-linearities: The droppers that connect the messenger and contact wires have zero-stiffness when they are under compression, a phenomenon known as slackening. Moreover, for high-speed vehicles, the small displacement assumptions regarding the wire movement depart from reality.
- Uncertainties: The catenary has some implicit uncertainties that highly affect the obtained results. The most important uncertainties are the deviation with respect of the nominal value of the mast height and dropper lengths, the initial sag of the contact wire at the

medium position between masts (some pre-sagging is usually introduced in catenary construction and/or renovation to improve the pantograph contact behaviour), the modelling and clamping condition of the registration arm and the contact stiffness between the collector and the contact wire.

The above features make difficult the catenary modelling with commercial software, and therefore most catenary models are developed from scratch as in-home codes. The catenary model used here is also implemented in an in-home code by Ceit, which is also its only user. The model is validated with the benchmark defined in EN 50318 [11], which assesses the correctness of the model at 250 and 300 km/h. The main features of the model are following listed:

- Wires modelling: Euler-Bernoulli beams finite element (FE) including geometrical stiffening due to mechanical tension.
- Droppers: Bar elements with slackening
- Registration arm: Linear spring-mass system
- Proportional damping is introduced into the wires and droppers
- Sliding contact: Penalty method
- Numerical integration: Newmark + Impulse methods
- Two contact wires can be considered (this disposition is frequent in DC systems to improve the distance between traction substations due to the reduced electrical resistance)
- Two-dimensional modelling of the catenary: It neglects the lateral dynamics of the catenary structure, despite considering the lateral shift of the contact position due to stagger.

2.3.1.2.1 Definition Of The Catenary And Pantograph Dynamic Model

The catenary is modelled as an in-plane structure, that means neglecting its lateral dynamic behaviour since according to [7] the two-dimensional modelling is suitable even at high speeds. Therefore, and accounting that the application of this model is for low and medium speeds, the assumption of an in-plane structure seems to be acceptable. The dynamic responses of the catenary and pantograph are obtained by solving the equation of motion of the system that reads

$$\begin{bmatrix} \mathbf{M}_c & 0 \\ 0 & \mathbf{M}_p \end{bmatrix} \begin{bmatrix} \ddot{\mathbf{q}}_c \\ \ddot{\mathbf{q}}_p \end{bmatrix} + \begin{bmatrix} \mathbf{C}_c & 0 \\ 0 & \mathbf{C}_p \end{bmatrix} \begin{bmatrix} \dot{\mathbf{q}}_c \\ \dot{\mathbf{q}}_p \end{bmatrix} + \begin{bmatrix} \mathbf{K}_c & 0 \\ 0 & \mathbf{K}_p \end{bmatrix} \begin{bmatrix} \mathbf{q}_c \\ \mathbf{q}_p \end{bmatrix} = \begin{bmatrix} \mathbf{f}_c \\ \mathbf{f}_p \end{bmatrix}. \quad (4)$$

The motion of catenary and pantograph are uncoupled, \mathbf{q}_c and \mathbf{q}_p , respectively. However, the right-hand term, which represents the forces loading both structures, contains the contact force that introduces the coupling between them.

2.3.1.2.1.1. Catenary System Matrices

The catenary model is formulated by using the geometrical features of the structure shown in Figure 11.

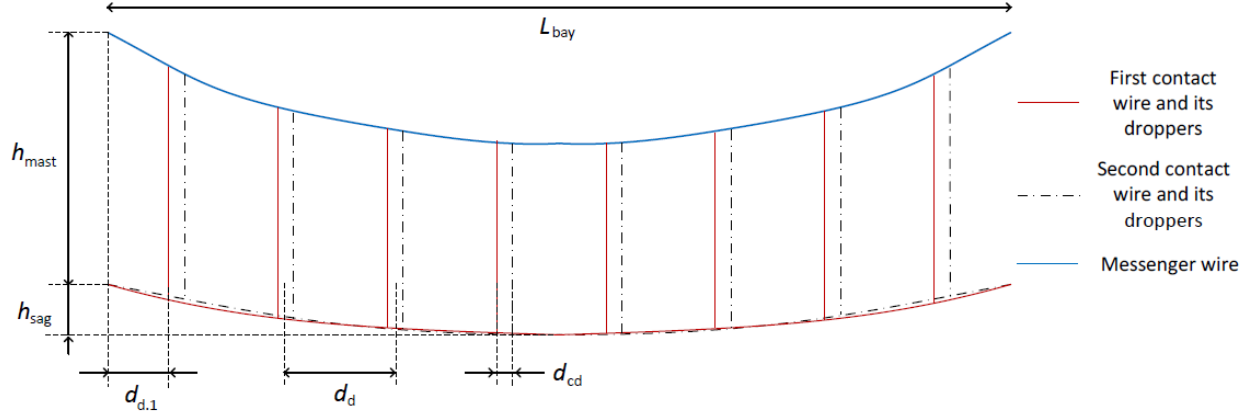


Figure 11 Basic scheme of a double contact wire catenary

The stiffness matrix of the catenary is defined as

$$\mathbf{K}_c = \begin{bmatrix} \mathbf{K}_{MW} + \mathbf{K}_d^{MM} & \mathbf{K}_d^{MC} \\ \mathbf{K}_d^{CM} & \mathbf{K}_{CW} + \mathbf{K}_d^{CC} \end{bmatrix} \quad (5)$$

where \mathbf{K}_{MW} and \mathbf{K}_{CW} are the messenger and contact wires matrices, respectively and \mathbf{K}_d refers to the droppers coupling both wires. The damping and mass matrices of the catenary have an analogous definition. The mass and stiffness matrices of the contact and messenger wires are built with Euler-Bernoulli FE, whose elementary matrices are

$$\mathbf{K}_{EB} = \begin{bmatrix} \frac{EA}{L} & 0 & 0 & -\frac{EA}{L} & 0 & 0 \\ 0 & \frac{12EI}{L^3} + \frac{6T}{5L} & \frac{6EI}{L^2} + \frac{T}{10} & 0 & -\frac{12EI}{L^3} - \frac{6T}{5L} & \frac{6EI}{L^2} + \frac{T}{10} \\ 0 & \frac{6EI}{L^2} + \frac{T}{10} & \frac{4EI}{L} + \frac{2TL}{15} & 0 & -\frac{6EI}{L^2} - \frac{T}{10} & \frac{2EI}{L} - \frac{TL}{30} \\ -\frac{EA}{L} & 0 & 0 & \frac{EA}{L} & 0 & 0 \\ 0 & -\frac{12EI}{L^3} - \frac{6T}{5L} & -\frac{6EI}{L^2} - \frac{T}{10} & 0 & \frac{12EI}{L^3} + \frac{6T}{5L} & -\frac{6EI}{L^2} - \frac{T}{10} \\ 0 & \frac{6EI}{L^2} + \frac{T}{10} & \frac{2EI}{L} - \frac{TL}{30} & 0 & -\frac{6EI}{L^2} - \frac{T}{10} & \frac{4EI}{L} + \frac{2TL}{15} \end{bmatrix} \quad (6)$$

and

$$\mathbf{M}_{EB} = \rho_l L \begin{bmatrix} \frac{1}{3} & 0 & 0 & \frac{1}{6} & 0 & 0 \\ 0 & \frac{156}{420} & \frac{22L}{420} & 0 & \frac{54}{420} & -\frac{13L}{420} \\ 0 & \frac{22L}{420} & \frac{4L^2}{420} & 0 & \frac{13L}{420} & -\frac{3L^2}{420} \\ \frac{1}{6} & 0 & 0 & \frac{1}{3} & 0 & 0 \\ 0 & \frac{54}{420} & \frac{13L}{420} & 0 & \frac{156}{420} & -\frac{22L}{420} \\ 0 & -\frac{13L}{420} & -\frac{3L^2}{420} & 0 & -\frac{22L}{420} & \frac{4L^2}{420} \end{bmatrix} \quad (7)$$

for the stiffness and mass, respectively. The damping elementary matrix is built from them assuming proportional damping as $\mathbf{C}_{EB} = \alpha_d \mathbf{M}_{EB} + \beta_d \mathbf{K}_{EB}$. Regarding the droppers, they are built with bar elements.

2.3.1.2.1.2. Definition Of The Pantograph Dynamic Model

The matrices concerning the pantograph are established by using a lumped mass model like the one shown in Figure 12. f_{sta} is the uplift force of the pantograph, which pulls up the system until

that force is balanced by the contact force. The uplift force is calculated as indicated by the standard EN 50367 [8] as

$$f_{sta} = 8.45 \cdot 10^{-4} V^2 + 100 \quad (8)$$

where V is the pantograph forward speed. Moreover, the dynamic behaviour of the pantograph collectors is introduced through their vibration modes. The collector vibration modes have been calculated by using a simplified model based on Euler-Bernoulli elements. The central part is modelled by an equivalent section that accounts for the graphite strip and the aluminium carrier. In both sides, the horns are introduced using beam element. A progressive change of the local coordinate system is also formulated to introduce the curvature of the horns. The pantograph stiffness matrix reads

$$\mathbf{K}_p = \begin{bmatrix} k_1 & -k_2 & 0 & \dots & 0 \\ -k_2 & k_2 & 0 & \dots & 0 \\ 0 & 0 & \mathbf{0}_{2 \times 2} & \dots & 0 \\ \vdots & \vdots & \vdots & \ddots & \vdots \\ 0 & 0 & 0 & \dots & \mathbf{0}_{2 \times 2} \\ \vdots & \vdots & \vdots & \ddots & \vdots \\ 0 & 0 & 0 & \dots & 0 \end{bmatrix} + k_3 \left(\mathbf{N}_{rg,r}^T \mathbf{N}_{rg,r} + \mathbf{N}_{rg,f}^T \mathbf{N}_{rg,f} + \mathbf{N}_{lf,r}^T \mathbf{N}_{lf,r} + \mathbf{N}_{lf,f}^T \mathbf{N}_{lf,f} \right), \quad (9)$$

where the ω^2 is a diagonal matrix with the squared value of the pantograph collector natural frequencies, and $\mathbf{N}_{rg,i}$ $\mathbf{N}_{lf,i}$ are the transformation vectors of the generalized coordinates to the relative displacement of the right and left springs (k_3). The damping matrix, \mathbf{C}_p , has an analogous structure to \mathbf{K}_p , but substituting ω^2 by the $2\omega\zeta$, where ζ is the modal damping vector of the collectors due to internal friction. The mass matrix of the pantograph reads

$$\mathbf{M}_p = \text{diag} \begin{bmatrix} m_1 & m_2 & m_3 & I_3 & 1 & m_3 & I_3 & 1 \end{bmatrix} \quad (10)$$

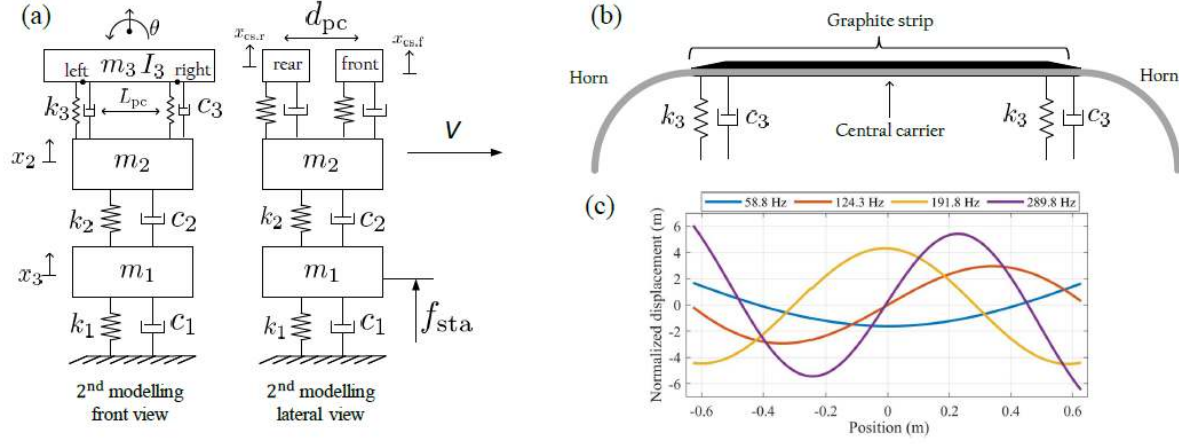


Figure 12 (a) Front and lateral views of the lumped mass model of the pantograph. (b) Scheme of the pantograph collector implemented design. (c) Normalized shape functions of the pantograph collector

The frequency response function of the pantograph gives us an initial insight into the dynamic response of this system and the effect of the collector modes. It is calculated, assuming a harmonic solution, as the ratio between the amplitude of the displacement and the exciting force

$$\mathbf{H}_p = \frac{\mathbf{Q}_p}{\mathbf{F}_c} = [-\omega^2 \mathbf{M}_p + i\omega \mathbf{C}_p + \mathbf{K}_p]^{-1} \quad (11)$$

The resulting frequency response function is shown in Figure 13. The excitation takes place at the central position of the collector and half-way between suspension and the central position. The first resonance taking place around 4.5 Hz is due to the vertical rigid solid motion of collectors over supports. The first vibration mode is significantly attenuated after installation, and the

reduction is even more important for the third and fourth modes. However, the second resonance remains almost unaltered due to supports act at the nodal positions of the vibration mode.

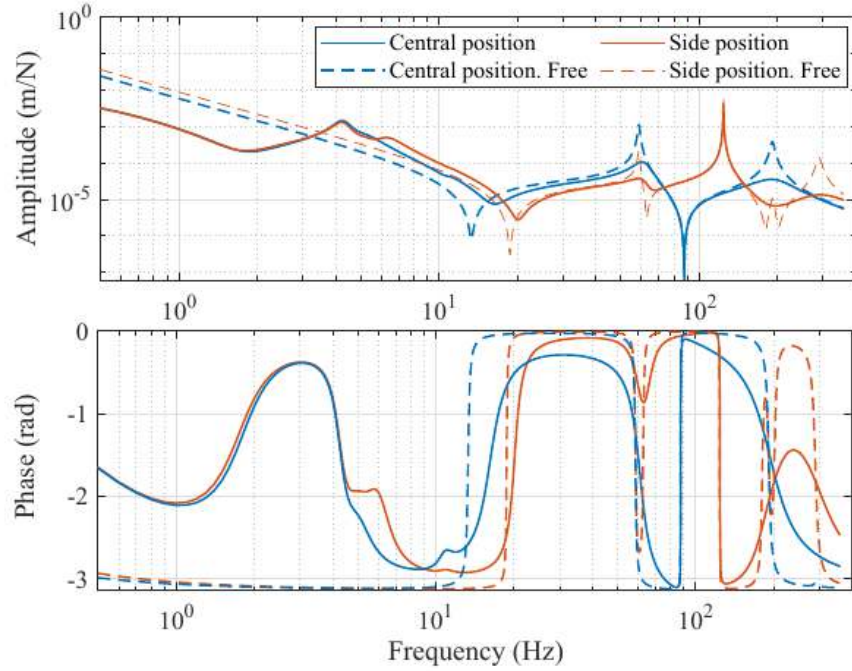


Figure 13 Predicted frequency response functions of the pantograph collector when they are installed and freely suspended. Solid line: Pantograph collector installed on the structure. Dashed: Pantograph collector freely suspended.

2.3.1.2.2 Catenary Initial Position Calculation

Normally, the features required for the definition of the FE building \mathbf{K}_{MW} and \mathbf{K}_{CW} are within the design values. The definition of \mathbf{K}_d requires the definition of the stiffness of each dropper that obeys $k_d = EA/L_d$. In some cases the length of the dropper, L_d , is not known. In this case, the calculation of the initial position follows the next steps:

- Firstly, the contact wire is studied separately from the rest of the structure. The forces due to the droppers holding the contact wire are unknown. To overcome this problem, a maximum deflection (pre-sag) of the contact wire at the mid-span in relation to the steady arms is defined. By using a parabolic distribution, the deflection of the contact wire at the dropper position is obtained. The static equation to solve is

$$\mathbf{K}_{CW}\mathbf{q}_{CW} = \mathbf{f}_d + \mathbf{f}_g \rightarrow \mathbf{q}_{CW} = \mathbf{F}_{CW}(\mathbf{f}_d + \mathbf{f}_g), \quad (12)$$

where \mathbf{F}_{CW} is the flexibility matrix and \mathbf{F}_d and \mathbf{F}_g are the dropper and gravity forces, respectively. The terms of \mathbf{q}_{CW} corresponding to the dropper positions are known, in that way, the number of unknown and equations are equalled.

- Secondly, the initial position of the messenger wire is obtained once the loading due to the dropper force is known.
- Thirdly, the dropper length can be calculated once the distance between wires is known as

$$L_d^i = \frac{q_{MW}^i + h_{mast} - q_{CW}^i}{\frac{f_d^i}{EA} + 1} \quad (13)$$

where q^i refers to the nodal vertical displacement at the positions of the i th dropper.

Figure 14 shows the initial position of CA-220 catenary [9]. In that figure, the height of mast supports and the dropper lengths are exactly the nominal, and therefore the static position of the span does not vary along the catenary. However, small departures from the nominal values commonly exist in reality. Figure 15 shows the static position of the catenary when certain randomness is introduced in the height of the mast supports and dropper lengths in relation to their nominal value.

2.3.1.2.3 Numerical Integration

To solve the catenary-pantograph interaction problem, firstly the coupling between pantograph and catenary must be defined. The coupling is due to contact forces and it is modelled with a penalty method. The i th contact force reads

$$f_{cont,i} = \begin{cases} K_{cont}\delta_i & \text{if } \delta_i > 0 \\ 0 & \text{if } \delta_i \leq 0 \end{cases} \quad (14)$$

where K_{cont} is the contact stiffness and $\delta_i = z_{p,i} - z_{c,i} - z_{irr,i}$ is the vertical interpenetration between catenary and pantograph at the contact positions, $z_{c,i}$ and $z_{p,i}$, respectively, which also introduces a term considering surface irregularities. If $\delta_i \leq 0$ a contact loss takes place and the contact force is zero, this fact introduces a non-linear behaviour in the problem.

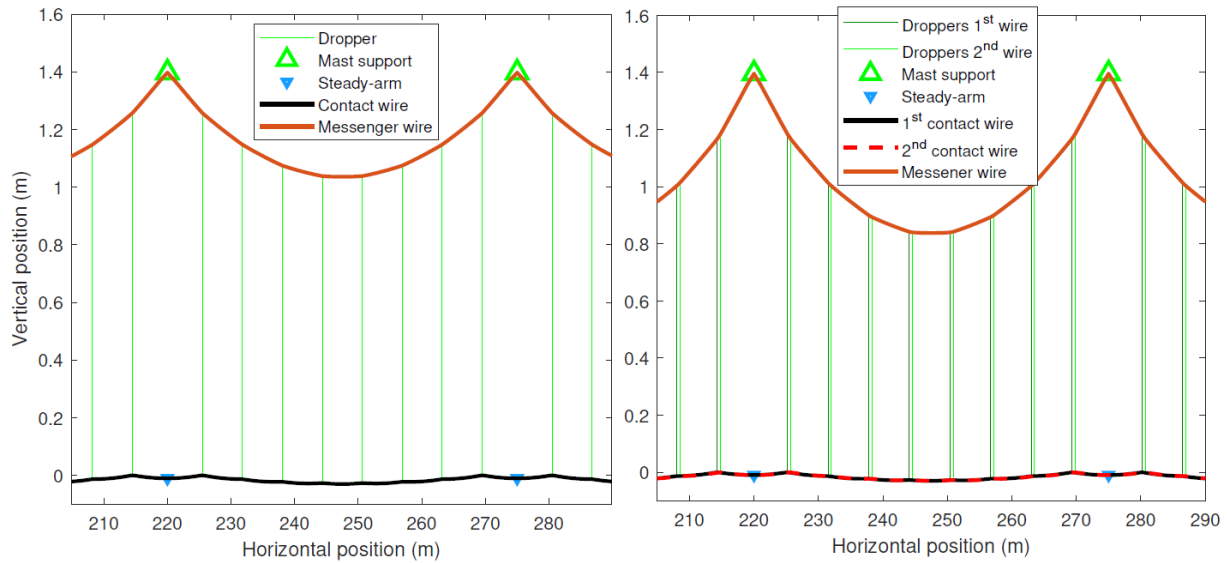


Figure 14. The initial position for the catenary type CA-220. One contact wire (left) and two contact wires (right). No uncertainties are introduced

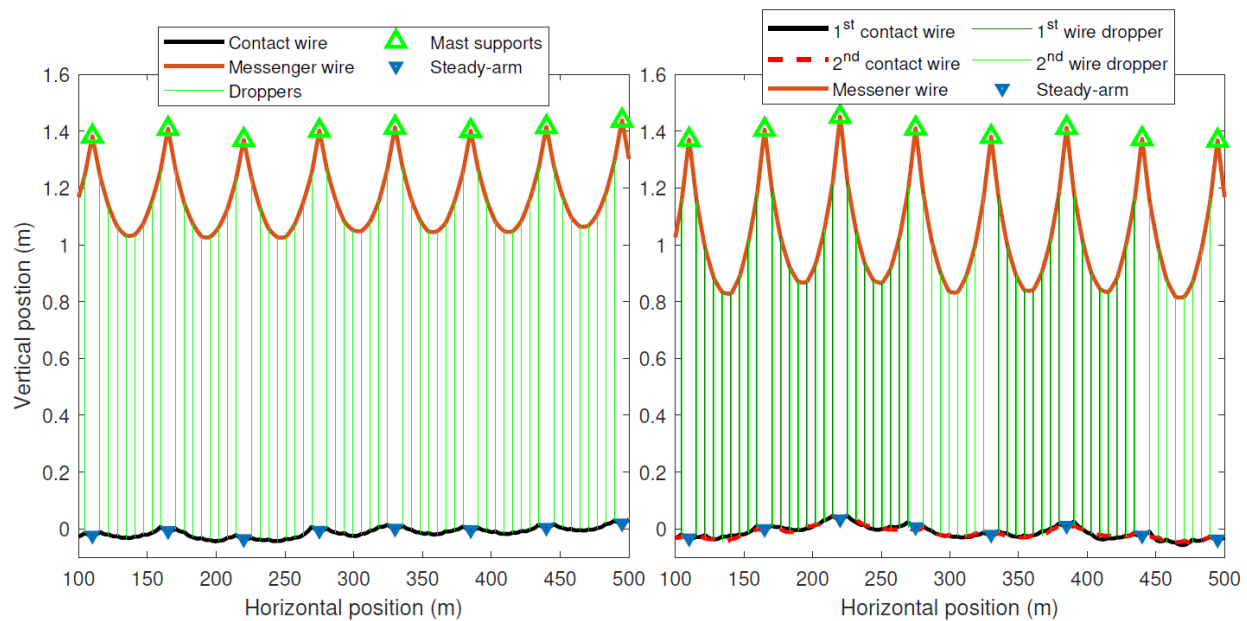


Figure 15. The initial position for the catenary type CA-220 considering uncertainties. One contact wire (left) and two contact wires (right). Randomness: $\sigma_s = 2$ cm and $\sigma_d = 6.6$ mm.

Another source of non-linearities is due to the droppers that in practice present an almost null stiffness when they are subjected to compression. This behaviour is known as slackening. Similarly to contact problem, slackening is modelled with a bi-linear stiffness. The elastic force of each dropper reads

$$f_{d,i} = \begin{cases} k_{d,i} (z_{d,i}^{mw} - z_{d,i}^{cw} - L_{d,i}) & \text{if axially loaded} \\ 0 & \text{if slackening} \end{cases} \quad (15)$$

where $z_{d,i}^{mw}$ and $z_{d,i}^{cw}$ are the vertical displacements of the messenger and contact wires at the clamping positions of the i -th dropper.

To avoid the continuous redefinition of the system equation due to dropper slackening, a balancing term is introduced into the left-hand side of Equation (4), which becomes

$$\begin{bmatrix} \mathbf{M}_c & \mathbf{0} \\ \mathbf{0} & \mathbf{M}_p \end{bmatrix} \begin{bmatrix} \ddot{\mathbf{q}}_c \\ \ddot{\mathbf{q}}_p \end{bmatrix} + \begin{bmatrix} \mathbf{C}_c & \mathbf{0} \\ \mathbf{0} & \mathbf{C}_p \end{bmatrix} \begin{bmatrix} \dot{\mathbf{q}}_c \\ \dot{\mathbf{q}}_p \end{bmatrix} + \begin{bmatrix} \mathbf{K}_c & \mathbf{0} \\ \mathbf{0} & \mathbf{K}_p \end{bmatrix} \begin{bmatrix} \mathbf{q}_c \\ \mathbf{q}_p \end{bmatrix} = \begin{bmatrix} \mathbf{f}_{bal} + \mathbf{f}_g + \mathbf{f}_{cont.c} + \mathbf{f}_{sd} \\ \mathbf{f}_{sta} + \mathbf{f}_{cont.p} \end{bmatrix} \quad (16)$$

where \mathbf{f}_{sd} refers to the slackened droppers, \mathbf{f}_g accounts for the gravity force, \mathbf{f}_{bal} imposes the initial position of the mast supports and the droppers and \mathbf{f}_{sta} is the uplift force of the pantograph. $\mathbf{f}_{cont.p}$ and $\mathbf{f}_{cont.c}$ are the projection of the contact over the catenary and pantograph structures, respectively. Equation (16) can be compacted and by using the Newmark's method its number of unknowns can be equalled to the number of equations as

$$\text{res}(\mathbf{q}_{\text{sys},k+1}) = \mathbf{A}_1 \mathbf{q}_{\text{sys},k+1} - \mathbf{M}_{\text{sys}} \hat{\mathbf{q}} - \mathbf{C}_{\text{sys}} \hat{\mathbf{q}} - \mathbf{f}_{\text{sta},\text{sys}} - \mathbf{f}_{\text{cont},\text{sys}} - \mathbf{f}_{\text{sd},\text{sys}} = 0 \quad (17)$$

In which the system displacements at the instant t_{k+1} are calculated in terms of the kinematic variables of the previous time step, t_k . The new terms in Equation (17) are

$$\mathbf{A}_1 = \frac{1}{\beta \Delta t^2} \mathbf{M}_{\text{sys}} + \frac{\gamma}{\beta \Delta t} \mathbf{C}_{\text{sys}} + \mathbf{K}_{\text{sys}} \quad (18)$$

$$\hat{\mathbf{q}} \equiv - \left[\frac{\gamma}{\beta \Delta t} \mathbf{q}_{\text{sys},k} + \left(\frac{\gamma}{\beta} - 1 \right) \dot{\mathbf{q}}_{\text{sys},k} + \left(\frac{\gamma}{2\beta} - 1 \right) \Delta t \ddot{\mathbf{q}}_{\text{sys},k} \right] \quad (19)$$

$$\hat{\mathbf{q}} \equiv - \left[\frac{\gamma}{\beta \Delta t^2} \mathbf{q}_{\text{sys},k} + \frac{1}{\beta \Delta t} \dot{\mathbf{q}}_{\text{sys},k} + \left(\frac{1}{2\beta} - 1 \right) \ddot{\mathbf{q}}_{\text{sys},k} \right] \quad (20)$$

where Δt is the time-step length and γ and β are Newmark integrator parameters. Equation (17) to (20) can be iteratively solved at each time-step by using a Newton-Raphson convergence method. However, the non-linear nature of $\mathbf{f}_{\text{cont},\text{sys}}$ and $\mathbf{f}_{\text{sd},\text{sys}}$ makes the direct numerical integration a slow choice to solve the pantograph-catenary interaction. It is due to the large number of DoF that catenary models normally involve. This issue can be overcome by taking advantage of the bi-linear nature of these non-linearities.

The methodology proposed by Gregori et al. [12] splits the solution into two components, one purely linear and another in which bi-linear terms are involved. The vector of generalized coordinates at the instant t is given by

$$\mathbf{q}_{\text{sys}}^t = \mathbf{q}_{\text{sys.kn}}^t + \sum_c^{n_{\text{cont}}} f_{\text{cont.c}}^t \begin{pmatrix} \mathbf{u}_{\text{cont.cat}}^{*c} \\ \mathbf{u}_{\text{cont.pan}}^{*c} \end{pmatrix} + \sum_d^{n_{\text{sd}}} f_{\text{sd.d}}^t \begin{pmatrix} \mathbf{u}_{\text{d.cat}}^{*d} \\ \mathbf{0} \end{pmatrix} \quad (21)$$

where $\mathbf{q}_{\text{sys.kn}}^t$ is obtained from the terms associated with the previous step and static behaviour in Equation (17). The contributions of the bi-linear terms are weighted by the impulse response of catenary and pantograph for excitations at contact and dropper positions. These impulse responses are denoted by the upper-script '*'. Introducing this definition of the displacement into the Equations (14) and (15), a reduced system is obtained that defines bilinear terms as

$$\begin{bmatrix} \mathbf{I}_{n_{\text{cont}}} - \mathbf{A} & \mathbf{B} \\ \mathbf{C} & \mathbf{I}_{n_{\text{sd}}} - \mathbf{D} \end{bmatrix} \begin{bmatrix} \mathbf{f}_{\text{cont}}^t \\ \mathbf{f}_{\text{sd}}^t \end{bmatrix} = \begin{bmatrix} \mathbf{E} \\ \mathbf{F} \end{bmatrix} \quad (22)$$

where \mathbf{I}_n is a $n \times n$ identity matrix. The iterative process is now limited to Equation (22), which is stopped once the contact positions and the slackened droppers do not change from one iteration to the next. In this way, the calculation of the non-linear terms involves an almost negligible computational cost. Once the force $\mathbf{f}_{\text{cont}}^t$ and \mathbf{f}_{sd}^t are known, the generalized coordinates are straightforwardly calculated according to Equation (21). The calculation of $\mathbf{q}_{\text{sys.kn}}^t$ is the most expensive process in terms of computational cost of this resolution procedure, which is calculated as

$$\mathbf{q}_{\text{sys.kn}}^t = \mathbf{J} \left[\mathbf{M}_{\text{sys}} \hat{\mathbf{q}} + \mathbf{C}_{\text{sys}} \hat{\mathbf{q}} + \mathbf{f}_{\text{sta.sys}} \right] \quad (23)$$

where $\mathbf{J} = \mathbf{A}_1^{-1}$ is the Jacobian matrix. This calculation must be performed once per iteration, and although the system matrices are constant along with the whole simulation, this operation becomes expensive in large models with around ten thousand degrees of freedom. Even so, this methodology makes affordable the calculation of a large number of simulations under different circumstances, since the computational cost is reduced in around two orders of magnitudes as compared with conventional resolution techniques.

2.3.1.2.4 The Convergence Of The Model And Validation

The model fulfils the requirement of standard EN 50318 [11] for its validation as shown in Figure 16 and Table 1. The convergence has been also analysed concluding that the error is kept below 1% for a sampling frequency of 2000 Hz and a FE discretisation of ten elements between adjacent droppers for both, messenger and contact wires. Figure 17 shows the power spectral density for different discretisation levels. Below 100 Hz, the solution with 10 FE between adjacent droppers matches the solution using 20 FE. A high level of accordance is achieved up to 200 Hz. Above that frequency the differences become noticeable.

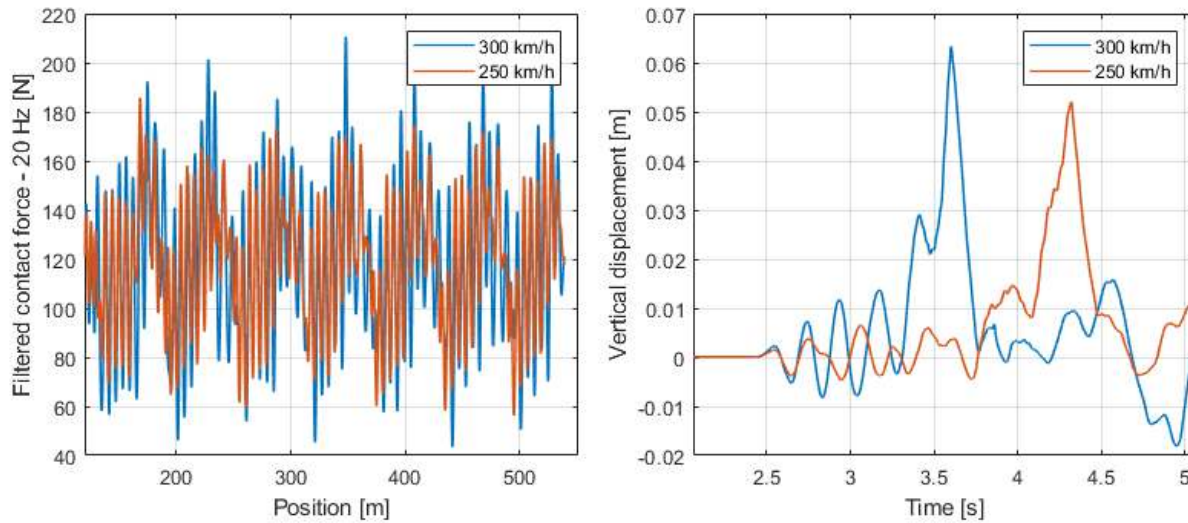


Figure 16 Time-domain results of pantograph catenary interaction with the parameters set according to EN 50318

Table 1 Ranges defined by the standard EN 50318 and results obtained with the model

	Ranges EN 50318		Results model	
	250 km/h	300 km/h	250 km/h	300 km/h
Mean force [N]	110 to 120	110 to 120	119.4	118.8
Standard deviation [N]	26 to 31	32 to 40	26.8	33.58
Maximum statical force [N]	190 to 210	210 to 230	199.9	219.6
Minimum statical force [N]	20 to 40	-5 to 20	38.9	18.1
Actual maximum statical force [N]	175 to 210	190 to 225	185.8	210.6
Actual minimum statical force [N]	50 to 75	30 to 55	56.2	43.3
Maximum uplift at support [mm]	48 to 55	55 to 65	51.2	63.3

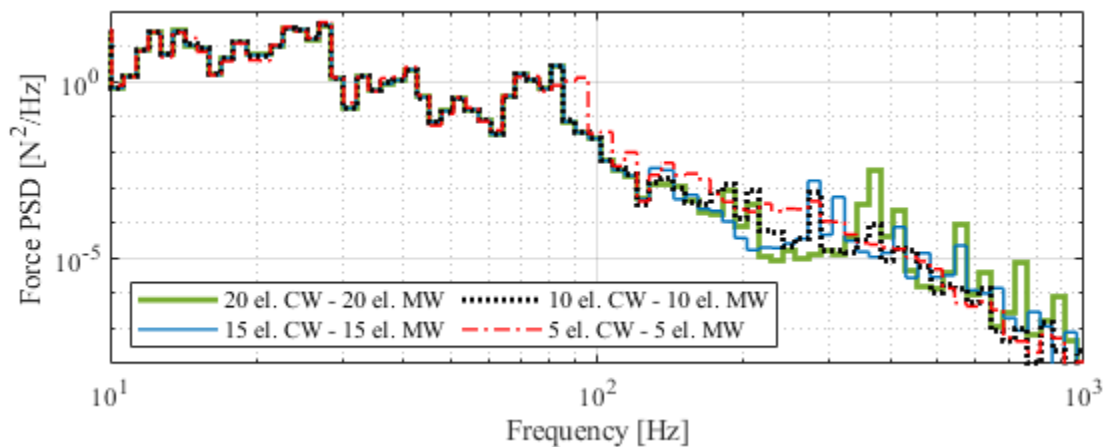


Figure 17 Power Spectral Density of the contact forces for different number of element modelling the wire within adjacent droppers

2.3.1.3 The Relation Between Acceleration and Contact Force

The improved numerical model is used to simulate the pantograph dynamic response at several speeds and different levels of uncertainties. The speeds cover the low and medium speed range, from 60 to 220 km/h. The uncertainties are defined in terms of the standard deviation of the dropper length and the mast height in relation to their nominal values. Three levels of irregularities are chosen:

- Level 1: $\sigma_d = 3.3$ mm and $\sigma_m = 1$ cm
- Level 2: $\sigma_d = 6.6$ mm and $\sigma_m = 2$ cm
- Level 3: $\sigma_d = 9.9$ mm and $\sigma_m = 3$ cm

The level two corresponds to the standard deviation of droppers length and mast height that is given in [12], which is chosen in the range presented in [13]. Therefore, level two represents the common deviation of mast and droppers. Level one would represent a highly accurate catenary installation, whereas level three is a defective configuration of the catenary, due to installation or deterioration.

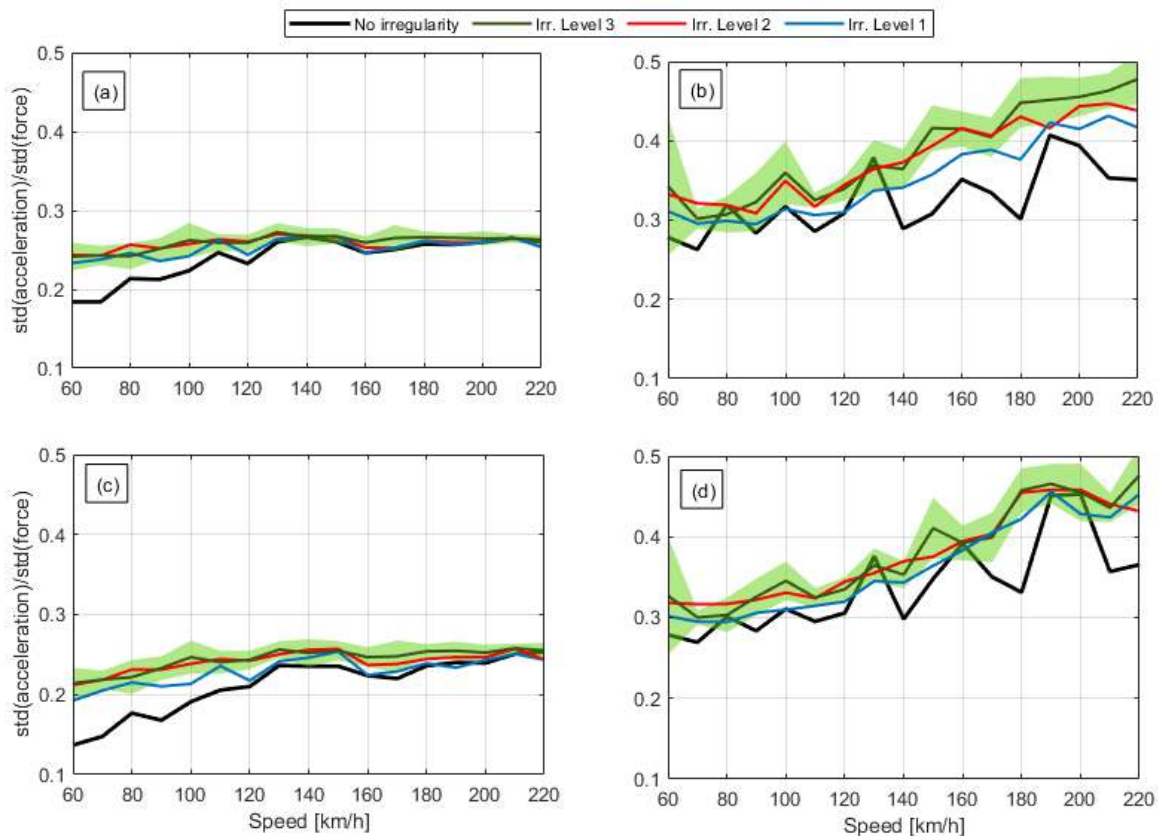


Figure 18 Ratio between the standard deviations of collector accelerations and the contact force. (a) Rear collector. Low-pass filter 20 Hz. (b) Rear collector. High-pass filter 20 Hz. (c) Front collector. Low-pass filter 20 Hz. (d) Front collector. High-pass filter 20 Hz.

Ten simulations are performed for each speed and each level of irregularity. The relation between the standard deviation of the pantograph collector accelerations and the contact forces are given in Figure 18. It also displays the ratio when no uncertainties are introduced. These results show a clear correlation between the standard deviation of the accelerations and the standard deviation of the force, which is almost constant on speed when the signal is studied below 20 Hz. This relation enables the estimation of the contact quality index according to EN 50367 if the uplift force of the pantograph is known. The catenary parameters correspond to the CA-220 type, with two contact wires and a separation between the mast of 55 m.

This ratio relating the collector accelerations and the contact forces will be used to estimate straightforwardly the contact force quality from the acceleration response.

2.3.1.4 Wear Model

2.3.1.4.1 Contact Wire

The wear model of the contact wire is taken from [14], which defines the worn material through

$$NWR = k_1 \left(\frac{1}{2} \cdot \left(1 + \frac{I_c}{I_0} \right) \right)^{-\alpha} \cdot \left(\frac{F_m}{F_0} \right)^\beta \cdot \frac{F_m}{H} + k_2 \frac{R_c(F_m) \cdot I_c^2}{H \cdot V} (1 - u) + k_3 \cdot u \frac{V_a \cdot I_c}{V \cdot H_m \cdot \rho} \quad (24)$$

where I_c is the current intensity, F_m is the contact force and R_c is the electrical resistance. The rest of the terms are constant parameters and their definitions can be consulted in [14]. The first, second and third terms in Equation (24) represent the mechanical, electrical and arc wear mechanisms, respectively. The wear is predicted in terms of the Normalized Wear Rate (NWR), which gives the worn material (mm³) per kilometre. The contact resistance is determined by an empirical relation as

$$R_c(F_m) = 0.013 + 0.09 \exp \left(\frac{14 - F_m}{11} \right) \quad (25)$$

2.3.1.4.2 Electromechanical Model

To solve equation (24) it is necessary to know the intensity of the electric current flowing for each contact position. Normally, there are four contact positions. For each one of the simulations referred to in the previous section, the current intensity flowing through the contact position, I_i , can be obtained by setting a value of the required current intensity by the vehicle, I , and solving the next system of differential equations for each time step

$$\frac{dI_1}{dt} = \frac{-(3R_1 \cdot I_1 - R_2 \cdot I_2 + R_4 \cdot I_1 - R_3 \cdot I_3 + R_4 \cdot I_2 + R_4 \cdot I_3 - R_4 \cdot I)}{4L_c} \quad (26)$$

$$\frac{dI_2}{dt} = \frac{-(3R_2 \cdot I_2 - R_1 \cdot I_1 + R_4 \cdot I_1 - R_3 \cdot I_3 + R_4 \cdot I_2 + R_4 \cdot I_3 - R_4 \cdot I)}{4L_c} \quad (27)$$

$$\frac{dI_3}{dt} = \frac{-(R_4 \cdot I_1 - R_2 \cdot I_2 - R_1 \cdot I_1 - 3R_3 \cdot I_3 + R_4 \cdot I_2 + R_4 \cdot I_3 - R_4 \cdot I)}{4L_c} \quad (28)$$

$$I = I_1 + I_2 + I_3 + I_4 \quad (29)$$

In turn, the demanded current intensity depends on the power supply required or delivered by the vehicle, calculated as

$$P = f_t \cdot V \cdot \eta \quad (30)$$

where f_t is the traction force and η is the efficiency of the traction equipment (transmission, motor, converters, etc.). The traction force is calculated as

$$f_t = M(a + g \cdot i) \quad (31)$$

where M is the vehicle mass, a is the acceleration, g is the acceleration due to gravity and i is the slope of the railway track.

Figure 19 shows the predicted contact force response, current intensity and contact resistance at each one of the four contact positions. Finally, the normalized wear rate is calculated at both contact wires according to the wear model proposed by [14].

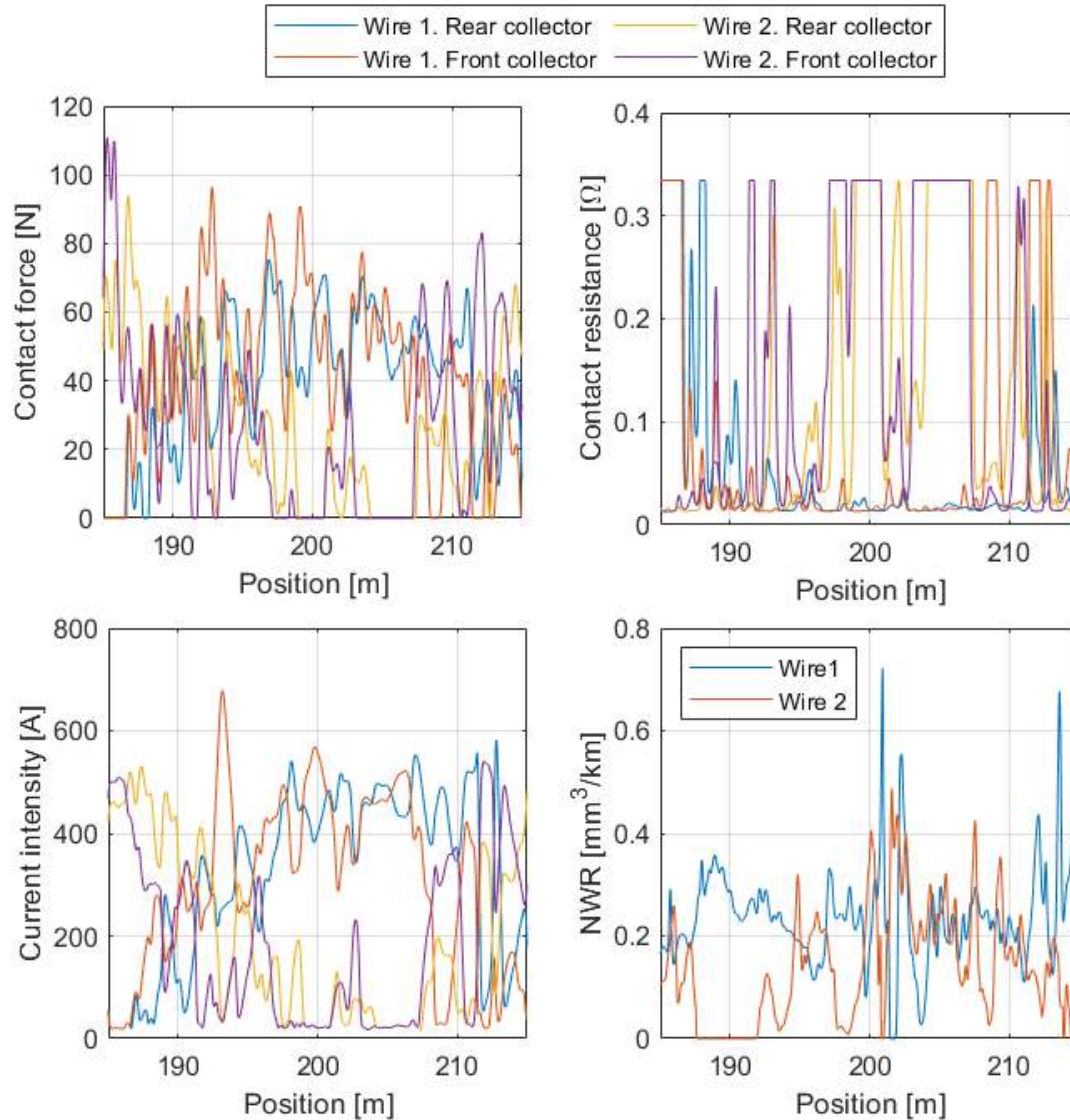


Figure 19 Predicted contact force, electrical resistance, current intensity and NWR for a vehicle travelling at 200 km/h, 1000 A as the total intensity demanded by the vehicle and level 2 of uncertainties.

2.3.1.4.3 Estimation of the Contact Wire Wear

The estimation of the wear on the contact wires is performed by using regression models which are trained with the simulated data. Regression models are trained to estimate the mean wear and maximum wear of the contact wire, employing as inputs the acceleration signals of the collector contact strips, the vehicle speed and the demanded or delivered current intensity. The maximum wear is given as a ratio between the maximum and mean wear values.

Figure 20 and Figure 21 show the predictions of the mean wear for the first and second contact wire, respectively, as well as the accuracy achieved by the prediction. Figure 22 shows the prediction of the ratio between the maximum and mean wear rates and the accuracy of the regression model.

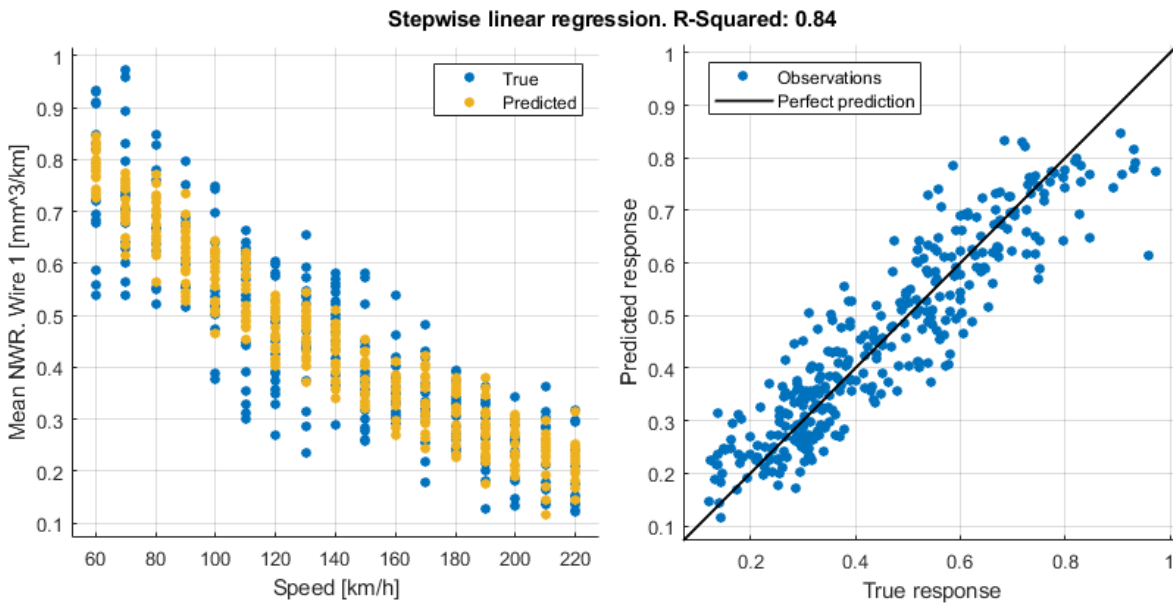


Figure 20 Estimation of the mean wire wear on the first contact wire (left) and accuracy of the regression model (right).

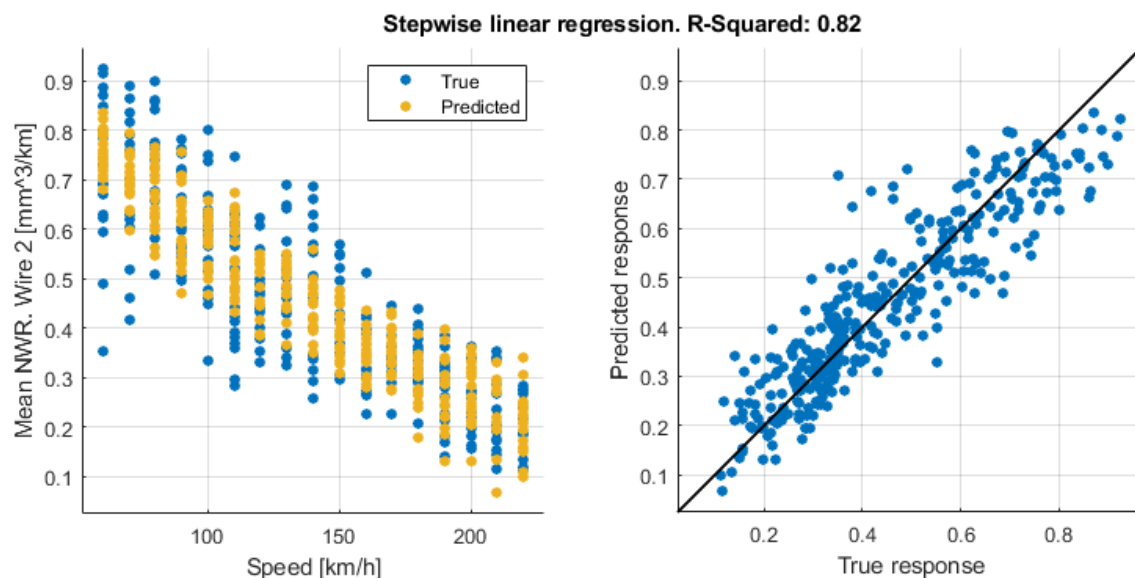


Figure 21 Estimation of the mean wire wear on the second contact wire (left) and accuracy of the regression model (right).

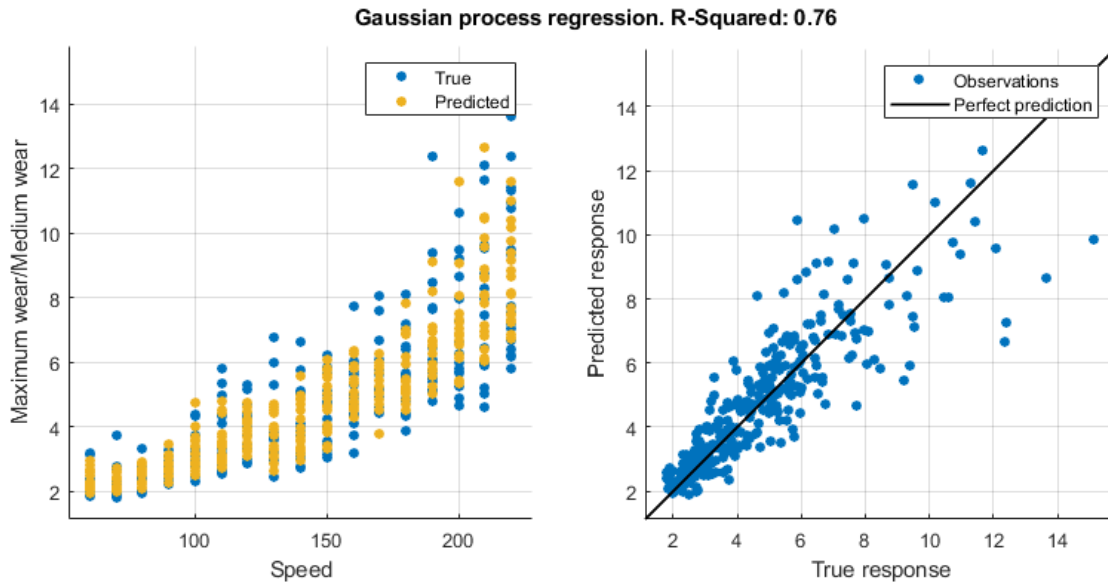


Figure 22 Estimation of the ratio between maximum and mean wear of the contact wires (left) and the accuracy of the estimation.

2.3.1.5 Overhead Contact Wire Geometry

The distance from the rails to the contact wire is the sum of:

- Vehicle's roof height.
- Pantograph's panhead height.

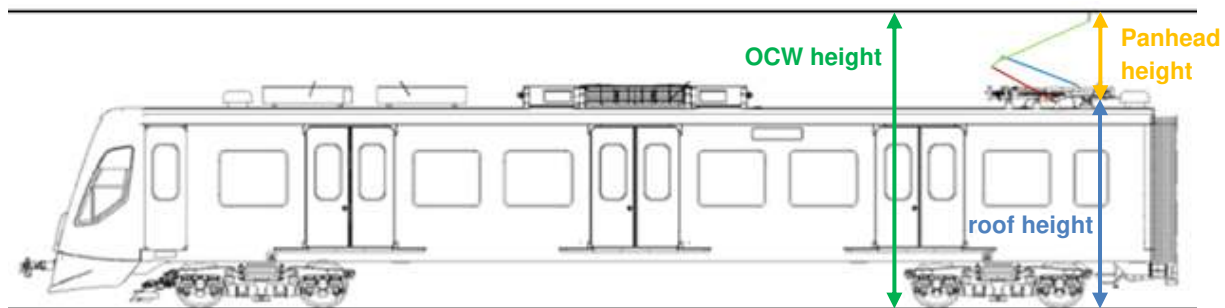


Figure 23. Distance from rail surface to contact wire

The pantograph's panhead height change to reach the contact wire while the distance of the roof remains around the same height.

The lower arm angle is monitored and the distance between the panhead and vehicle's roof is obtained employing a linear (or quadratic) equation. The overhead contact wire height is obtained adding the obtained value to the height of the vehicle's roof.

The obtained results will change for different units due to the difference in wheels' radius. From new to worn profiles, wheels' radius can change around 30-50 millimetres but shows slow progress over time. If relative contact wire height is measured from a reference point, the effect of wear on wheel profile is neglected.

2.4 Conclusions

In this chapter, an in-deep work is presented regarding the modelling of both pantograph and catenary. Concerning the pantograph, the kinematic model of the main structure fits the result experimentally measured, this allows the estimation of the height and applied torque by knowing inclination of the lower arm. In addition to the kinematic model, the relationship between a static contact force on the panhead and an applied torque on the lower arm is assessed. Moreover, the pantograph model has been extended to approach its dynamic behaviour with a lumped mass system. Regarding the catenary, a dynamic model is proposed to study the dynamic interaction between the catenary and pantograph, whose validity is guaranteed by standard EN 50318 [11]. The mentioned standard refers to single contact wire catenary, but the developed model is extended to more common double contact wire catenaries. The catenary model allows studying the expected response of accelerometers in the pantograph. This analysis makes possible to choose the best position for the accelerometers, to establish relations between the measured acceleration and the contact forces, and to point out zones more prone to develop wear.

2.4.1 The Impact of E-GNSS

The models described in section 2 have been developed for the extraction of different KPIs by means of different sensors placed on the pantograph. These KPIs are calculated at different track locations and dates. The output of sensors depends on sensibility and repeatability and then are post-processed with a slight inherent error within the algorithms. Thanks to the use of E-GNSS the raw data obtained from sensors to feed the algorithms (further processed by SIA_POS) provide a precise position (<1m as for KP). Therefore, deviation from miss-positioned points is neglected. E-GNSS strengthens the reliability of developed models reducing the amount of necessary data (e.g. filtering, alignment, etc.) for the prognosis of health assessment: e.g., a single value (per KPI) per KP per day would be enough to assess the condition of the catenary, despite a continuous data collection with position information that is used for the generation of real-time events.

3 iPantMon Health Status Assessment

3.1 Description of iPantMon Health-Related KPIs According To The Use Cases

According to the definition of use cases of deliverable D2.1, those related to the health status assessment of the pantograph are

- Use case #3: wear of contact strips

Also, KPIs related to the interaction of the pantograph-catenary system are relevant for iPantMon:

- Contact force
- Vertical displacement of the contact point
- Shocks

3.1.1 Wear Of Contact Strips

Wear modes of current collecting materials were empirically classified into mechanical wear and electrical wear modes. The mechanical wear mode is thought to be caused by adhesive and abrasive wear under high contact load conditions, whereas the electrical wear mode is thought to be caused by electric arcs under contact loss conditions. The wear rate of current collecting materials increases significantly due to electric arcs. Wear reduction measures have therefore been proposed to prevent contact loss by improving dynamic interaction between the catenary and the pantograph.

3.1.2 Pantograph-Catenary Interaction

The KPIs associated with the pantograph-catenary interaction that are visualized in iPantMon are the same as those visualized in iCatMon. See section 2.1.4 for the correspondent description.

3.2 Description of Inputs

The inputs and measured signals that are used to assess the health-related KPIs of the pantograph and its interaction with the OCW are the same as those used for iCatMon. See section 2.2 for the correspondent description.

3.3 Description Of Health Assessment Methodology

3.3.1 Pantograph-Catenary Interaction Assessment

The KPIs corresponding to the interaction between the pantograph and catenary systems relevant to iPantMon are the same as those described in the previous chapter for iCatMon.

3.3.2 Estimation Of The Contact Strip Wear

The wear on contact strip is studied by the shifting of the collector natural frequencies. As the graphite of the contact zone is removed, the natural frequencies of the collector vary. Figure 24 shows the shifting of the natural frequencies included in Figure 12 as the graphite strip is worn. The spectral analysis of the acceleration signal will reveal the location of the natural frequencies of the collector, and by using the trends of Figure 24 and estimation of the percentage of worn graphite can be made.

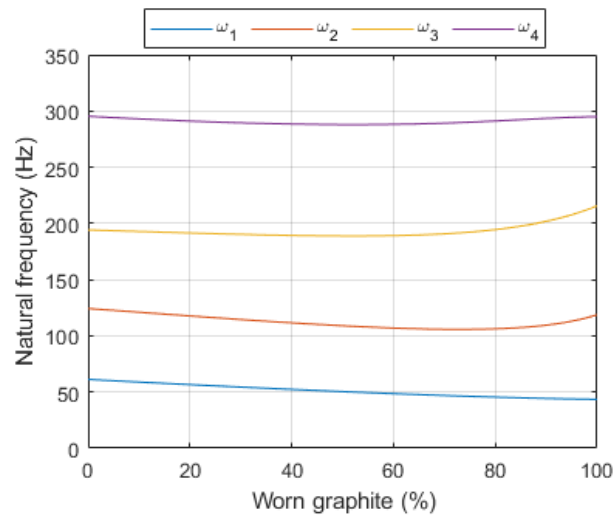


Figure 24 Change of the value of the natural frequencies of the collector as the graphite is worn

3.4 Conclusions

In this chapter, the in-deep work presented in section 2 is applied regarding the modelling of both pantograph and catenary. Besides, to estimate the contact strip wear, the dynamic behaviour of the collectors is also modelled and their natural frequencies are estimated for rates of worn graphite. A shifting of the natural frequencies was detected that can be used for assessing their status.

3.4.1 The Impact of E-GNSS

Different KPIs are calculated with the developed pantograph and catenary models. As occurs with iCatMon, E-GNSS reduces the amount of required data for health status assessments. This is due to the precise position of acquired data for later analysis (see section 2.4.1) for those KPIs that are referred to the pantograph to catenary interaction.

4 iWheelMon Health Status Assessment

4.1 Description of iWheelMon health-related KPIs according to the use cases

According to the use cases defined in deliverable D2.1, the following two-wheel defects are considered in this project:

- Wheel flats
- Polygonization wear

4.1.1 Wheel Flats

Wheel flats are localized wheel defects that are typically a result of wheel locking during braking. The wheel blocking is a consequence of insufficient adhesion between wheels and rails [15]. Flat wheels generate impact forces that can cause severe damage to the railhead surface. Additionally, they produce disturbing noise affecting the comfort of passengers and people living adjacent to railway tracks.

4.1.2 Polygonization Wear

Polygonization wear or polygonalization is the process of growth of out-of-round (OOR) profiles of the wheels [16]. This type of periodic OOR irregularity has been detected especially on disc-broken wheelsets on high-speed trains [17]. Polygonization wear can be characterised by the wavelength of the irregularity (number of harmonics around the wheel circumference) and its amplitude. The dominating harmonics of polygonal wheels typically range from one to five wavelengths around the wheel circumference [18], while the amplitude is of the order of 1 mm [17]. Figure 25 shows an example of polygonization wear on an ICE wheelset with three dominating harmonics (taken from [19]). To maintain the roundness of the wheels, wheel reprofiling is carried out periodically. Different reprofiling strategies have been suggested in the literature. In [20] it is suggested, based on a numerical simulation of wheelset wear on an Italian fast passenger train, to reprofile the wheel after about 200,000 km.

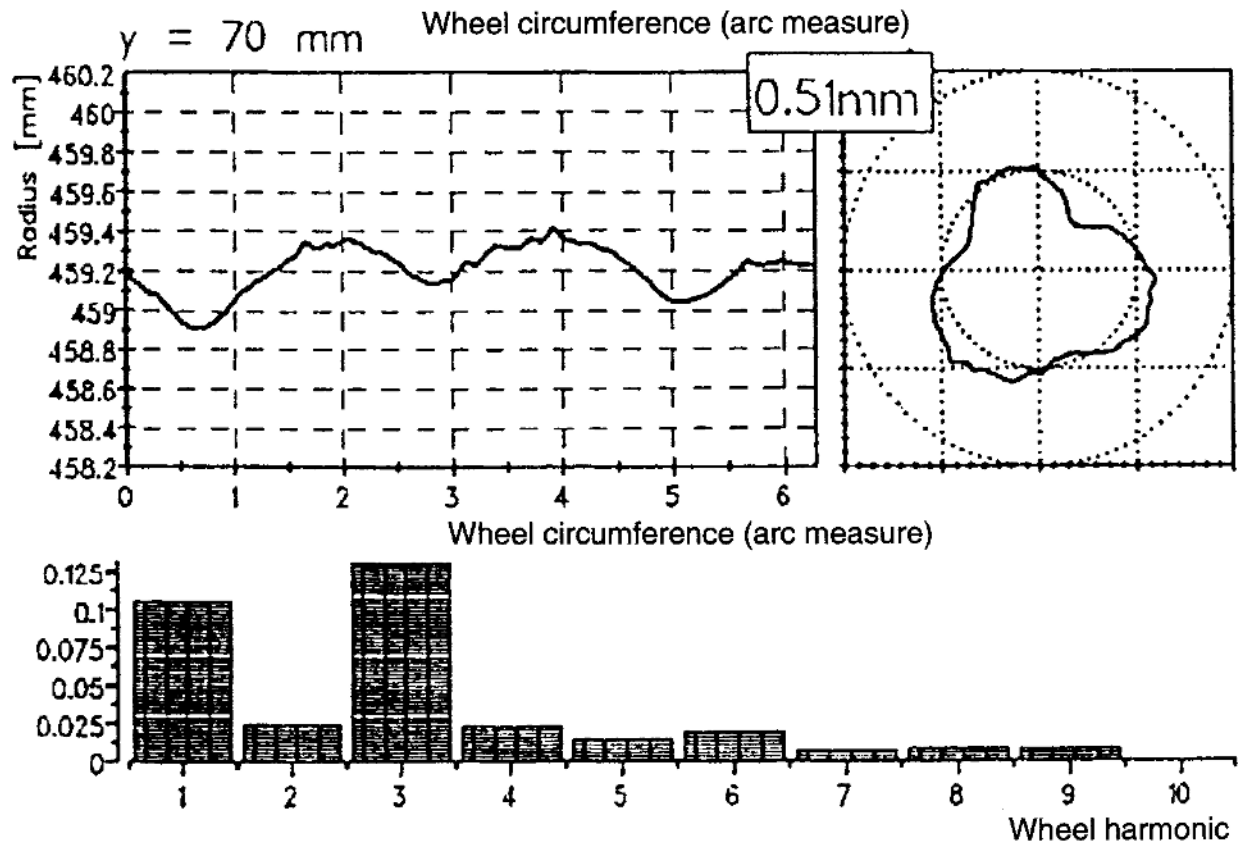


Figure 25. Polygonization wear of a solid steel wheel with three dominant harmonics around the wheel circumference. The bars indicate the distribution of different harmonics. (Taken from [5].)

Non-binding limits for OOR of wheels are specified in the EN15313 standard [21] based on e.g. visual inspection and impact loads measured with trackside wheel impact load sensors based on either strain gauges or accelerometers.

Wheel diameter — dependent speed	Permitted Out-Of-Roundness (Δr)
$D > 840 \text{ mm}$ <ul style="list-style-type: none"> $v_{\max} \leq 60 \text{ km/h}$ $60 \text{ km/h} < v_{\max} \leq 160 \text{ km/h}$ $160 \text{ km/h} < v_{\max} \leq 200 \text{ km/h}$ $v_{\max} > 200 \text{ km/h}$ 	<p>1,5</p> <p>1,0</p> <p>0,7</p> <p>0,5</p>
$380 \text{ mm} < d \leq 840 \text{ mm}$ <ul style="list-style-type: none"> $v_{\max} \leq 200 \text{ km/h}$ $v_{\max} > 200 \text{ km/h}$ 	<p>0,7</p> <p>0,5</p>
$d \leq 380 \text{ mm}$	0,3

Figure 26. Permitted deviation from roundness according to Annex I of EN15313 [7].

Reprofiling strategy: Current wheel reprofiling strategies (as carried out by e.g. FCG) are based on periodic reprofiling carried out once the wheels have run a certain number of kilometres. Through this continuous recovering of the wheel profile the life of the wheels can be extended. This procedure is complemented with periodical checks of the wheel profiles with different measurements of the control values of the profile, if any value overtakes the limits, a corrective reprofiling in order to recover the nominal profile is performed.

4.2 Description of Inputs

The following sections describe the physical parameters that describe the different wheel failure types and the signal measured with the SIA on-board measurement system.

4.2.1 Physical Parameters

Wheel flats and OOR wheels cause periodic impacts. The resulting excitation frequency f depends on the train speed v , the wheel circumference C and the number of dominating harmonics N :

$$f = \sum_{h=0}^{h=N} \frac{h \cdot v}{C} \quad (32)$$

4.2.2 Measured Signals

The SIA_ABA on-board sensor system is described in detail in Deliverable D 4.1. The system measures the vertical, longitudinal and lateral acceleration at the axle-box. The wheel-failure modes investigated in this project according to the use cases specified in Deliverable D2.1 mainly influence the vertical component of the ABA data.

4.3 Description of Health Assessment Methodology

The presence of a wheel flat causes periodically recurrent impacts on the wheel on the track at a constant covered distance equal to the wheel circumference which in turn provokes vibrations of the vehicle. At constant speed, these regularly appearing excitations take place at constant time differences. In this case, the system is periodically excited by similar input impulses which are reflected in the acceleration signal at the axle box by the regular presence of the impulse response of the vehicle at constant time differences. Theoretically, this is described by the convolution of the impulse (which is, as a function of time, a sum of Kronecker Delta functions whose first arguments are multiples of T when the impulse occurs at time differences of length T) and the system response (Figure 27). Analogously the acceleration signal can be represented as a function of distance instead of time and the impulse caused by a wheel flat occurs in equal distance differences L . For the rest of this section, these two mentioned functions are denoted by f and g and their convolution is called h .

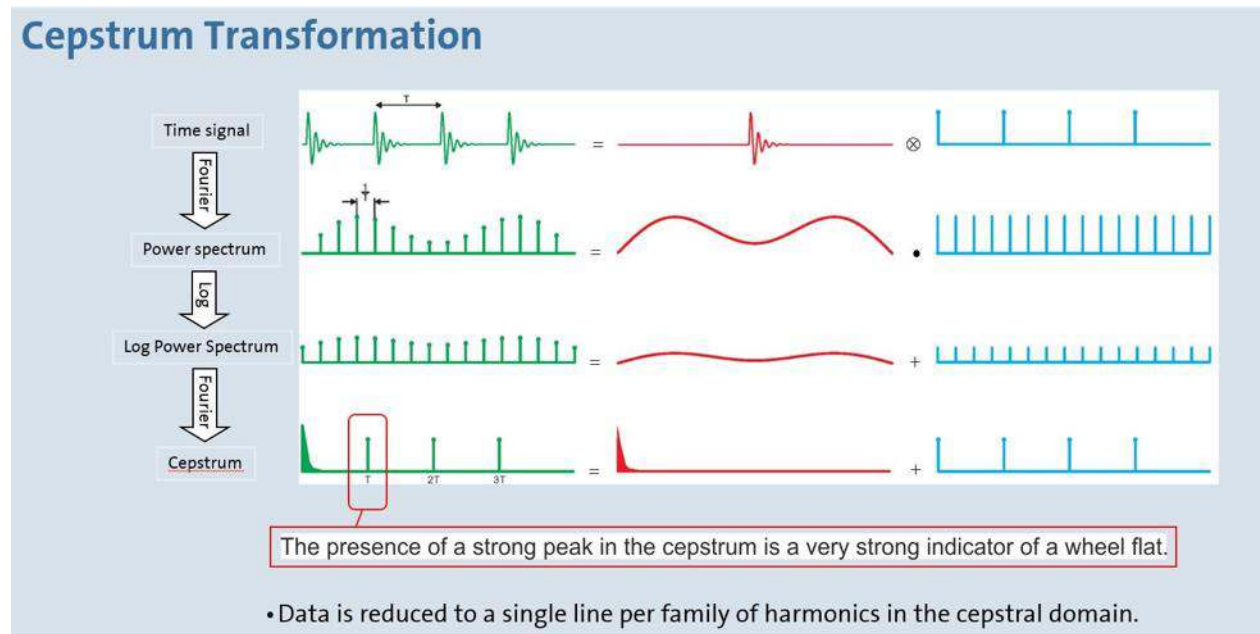


Figure 27. Cepstrum analysis of a periodic excitation caused by a wheel flat.

To recover the wheel flat impacts, the acceleration data is transformed by computing the Fourier Transform, taking the logarithm of its squared absolute values, transforming the logarithm of this power spectrum to its Inverse Fourier Transform and finally taking its squared absolute values.

This is explained in the following paragraph by only focusing on the part of the acceleration signal described above.

The Fourier Transform $F(h)$ of the convolution $f * g$ of the two functions f and g is given by the product $F(f) \cdot F(g)$ of the two Fourier Transforms of f and g . The function f is periodic on a finite interval with period T and its Fourier Transform is nonzero only for multiples of $1/T$ taking the same values. Passing to the Power Spectrum, i.e., the squared absolute values of the Fourier Transform is commutative with multiplication and transforms the output to the real range. The transition from the Power Spectrum to its logarithm divides the parts coming from f and g into a sum. The function $\log(|F(h)|^2)$ equals the sum of the corresponding terms related to f and g :

$$\log(|F(h)|^2) = \log(|F(f) \cdot F(g)|^2) = \log(|F(f)|^2) + \log(|F(g)|^2) \quad (33)$$

Adding a constant to $|F(f)|^2$ avoids zero-valued input to the logarithm but does not change the periodicity of the data; it will only be reflected in the value of the Inverse Fourier Transform at argument 0. Similarly taking the logarithm of $|F(f)|$ only affects the magnitude of the peaks in the output of its Inverse Fourier Transform but not the fact of their presence. Since mapping, a function to its Fourier Transform as well as to its Inverse Fourier Transform are linear operators, the Inverse Fourier Transform of $\log(|F(h)|^2)$ is given by the sum

$$F^{-1}(\log(|F(h)|^2)) = F^{-1}(\log(|F(f)|^2)) + F^{-1}(\log(|F(g)|^2)) \quad (34)$$

The function $\log(|F(f)|^2 + c)$ is periodic with length $1/T$ and its Inverse Fourier Transform is periodic with length T and zero at non-multiples of T . Since $F^{-1}(\log(|F(f)|^2))$ constitutes one of the summands in the expression $F^{-1}(\log(|F(h)|^2))$, the peaks in the amplitudes of the former function coming from the periodic wheel flat impulses should be visible in the latter function, too. The last step, the transition from $|F^{-1}(\log(|F(h)|^2)|$ to its squared values (the Power Cepstrum), keeps local maxima.

The measured data is processed as follows. The speed and its time information are examined to find time windows of nearly constant speed with a minimum length of 15 seconds. The axle box acceleration data is recorded at a constant sampling frequency of 20000 Hz and is synchronised with the speed by their time vectors. Since small deviations in speed in a window up to 1.2 m/s are tolerated, the axle box acceleration data is represented as a function of distance instead of time. The speed information is used to calculate the covered distance at each timestamp of the acceleration data. The acceleration data is then interpolated to constant sampling frequency in the distance domain.

Using the acceleration data of the constant speed window, Short Time Fourier Transform (STFT) is performed with a window length of 262144 data points which corresponds to approximately 13 seconds of data. Then for each window, the logarithm of the Power Spectrum is taken as input to compute its Discrete-Time Inverse Fourier Transform. The Power Cepstrum is finally given by the squared absolute values of the output.

At the presence of a wheel flat, a local peak in the Power Cepstrum at the argument of the wheel circumference is expected. Thus, for each window, the maximum of the Power Cepstrum of arguments in the domain 1 m to 35 m and its argument are extracted. For the whole window of constant speed, this information is reduced to the median of the arguments of the maxima in each window of 13 seconds and the mean of the maximal values.

Poligonalisation is expected to increase the amplitude of the higher-order harmonics compared to the fundamental mode and can hence be quantified by the relation of the amplitude of the harmonics compared to the fundamental amplitude.

4.4 Results And Conclusions

Figure 28 and Figure 29 show results obtained by the described methodology using data measured on a measurement train of Austrian Federal Railways (ÖBB) in June 2019. Figure 28 shows the Power Cepstra calculated based on sub-windows of 13 seconds length within a nearly constant speed window with an average speed of 27.34 m/s. The vertical red dotted line marks the median of the arguments of the maximal value in the quefrequency domain 1 m to 35 m (the figure only shows the subsection from 1 m to 15 m).

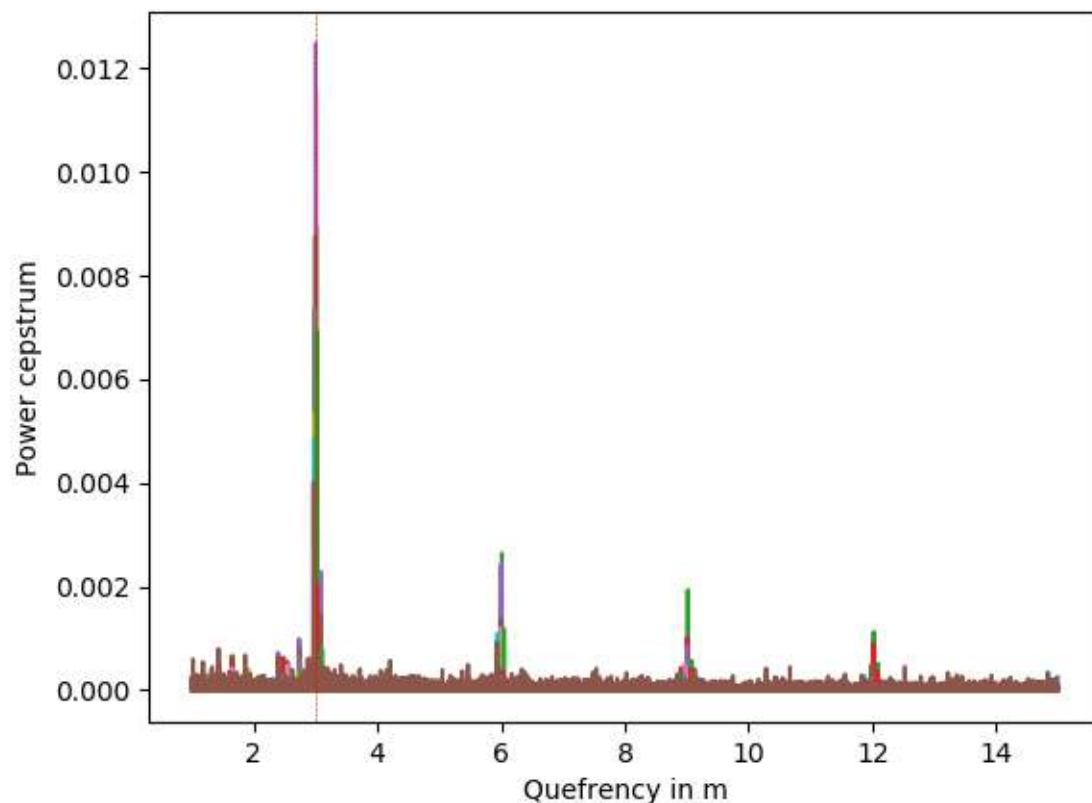


Figure 28. Power Cepstrum in the quefrequency domain from 1 to 15 m of axle box acceleration data at an average window speed of 27.34 m/s. Different colours represent the Power Cepstra of the different windows of approximately 13 seconds of data.

Figure 29 shows the analogue for another window where the driving speed was approximately 13 m/s. The median value of the arguments of the local maxima in the domain 1 to 35 m is found at a value of approximately 3 meters which is assumed to be the wheel circumference which indicates the presence of a wheel flat.

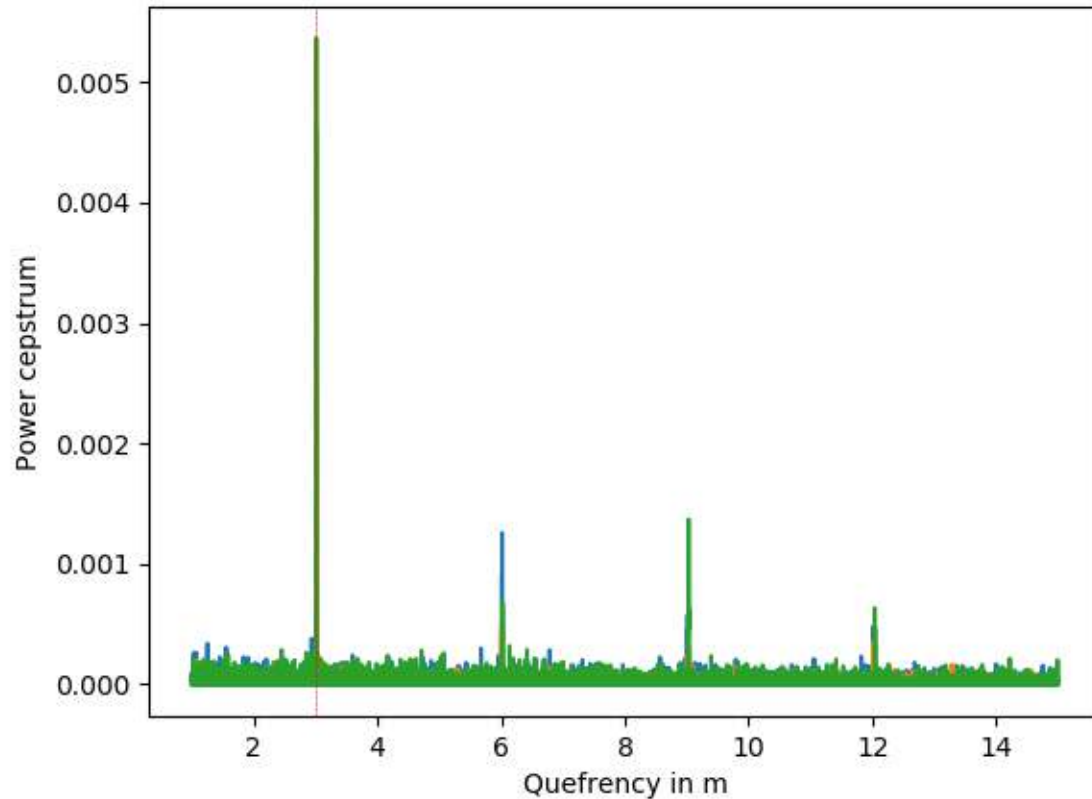


Figure 29. Power Cepstrum in the quefrequency domain 1 to 15 m of axle box acceleration data at an average window speed of 13.04 m/s.

4.4.1 The Impact of E-GNSS

The methodology described in section 4.3 strongly relies on the speed information from the SIA_POS system in two ways. Firstly, the data is split into segments of similar speed. If the speed time series provided by SIA_POS shows larger gaps, windows with constant speed and the appropriate length may be hard to find. Secondly, if the speed information is inaccurate because of these gaps or other inaccuracies in the measurements, the transformation from time to distance domain suffers. This may result in weaker peaks in the Cepstrum and hence leads to flawed information on the wheel health status.

Within SIA it was shown that the use of E-GNSS is beneficial by providing an increased number of visible satellites in the challenging rail environment (see deliverable D3.2). This effect is reflected in an increased satellite count when a higher elevation mask is applied and in the dilution of precision (DOP) parameters, which relate to the quality of the best obtainable positioning solution.

Therefore, the use of E-GNSS increases the accuracy of the speed estimation provided by the SIA_POS system. Increasing the accuracy of the speed estimate by 1 % also increases the accuracy of the wheel diameter estimate by 1 %. Specifically, for a wheel with a diameter of 1 m, this means that a 1 % improvement in accuracy leads to an absolute improvement of 10 mm, which corresponds to the expected wear at a mileage of approx. 100,000 - 300,000 km. Consequently, there is a direct bearing of E-GNSS on the success of the wheel monitoring and wheel health status assessment.

5 iRailMon Health Status Assessment

5.1 Description of iRailMon Health-Related KPIs According to the Use Cases

Two main groups of track defects can be distinguished based on their wavelength. The first group is considered as track geometry defects with a typical wavelength longer than 2 m. The second group comprises short-wavelength track defects such as corrugation and isolated track defects. The defects in the latter group are investigated in this project according to the KPIs defined in deliverable D2.1.

5.1.1 Rail Corrugation

Rail corrugation is a wave-type wear of the rail surface due to traffic load with a wide variety of wavelengths. We can distinguish between two types, short-pitch and long – pitch corrugation. Corrugation shows as an undulation of the rail surface with typical wavelengths between 0.03 – 0.3 m.

Short-pitch corrugation is characterized by a pseudo-periodical sequence of bright ridges and dark hollows on the running surface (Figure 30). The pitch generally varies between 0.03 and 0.08 m.



Figure 30. Example of short-pitch corrugation.

Long-pitch corrugation is characterized by depressions in the running surface which are more or less pronounced and uneven in relation to an ideal rectilinear profile. There is no difference in appearance between ridges and hollows. The pitch generally varies between 0.08 and 0.3 m approximately.

Long-pitch corrugation generally occurs on the inside stretches of curves, and it is most common on suburban and underground railways.

Conventional means of detection:

- Visual and sonic observation

- Observations based on measurement recordings carried out track inspection vehicles
- Observations based on measurement recordings carried out purpose-build vehicles

Recommendations for maintenance:

Grind rails where corrugation is on a scale prejudicial to:

- Track maintenance
- The running gear of vehicles
- The environment (high level of noise due to passing trains)

Maintenance strategy:

The treatment most commonly adopted for existing corrugation is to grind the rail and straighten welds, thereby minimizing the initial roughness which excited vibration of the vehicle on the track shiftiness and gives rise to high dynamic loads.

The strategic proposed is that after a corrective grinding a cyclical grindings campaign should be designed in order to extend the lifespan of the rails.

An initial grinding should always be done over the new rails installed, in order to delete residuals defects, then a cycle grinding as we have said will be necessary to keep the rail in the better conditions for a long time, but it's true that we should take care that a cyclic or corrective grinding with only partial damage removal may mask deeper damage until spalling occurs.

The introduction of cyclic grinding implies a change of the current maintenance strategy, in particular the passage towards predictive maintenance instead of corrective or palliative maintenance. At the same time, preventive grinding contributes to the industrialization of infrastructure maintenance.

5.1.2 Short-wave Irregularities

Squats are a rolling contact fatigue phenomenon which occurs mainly on straight lines with high shear stresses, especially zones where the wheel-rail adhesion is strongly demanded. Modern high power rolling stock with ABS and spin – control devices worsen the situation. As the squats are caused by high contact stresses in the wheel-rail contact patch, track design (Stiffness, gradient) and maintenance of the running band on the top of the rails are very important to reduce the number of squats.



Figure 31. Examples of squats on the running surface of the railhead.

Squats often occur at welds due to poor geometry of running band.

This defect is visible on the running surface of the rail head as a widening and a localized depression of the rail/wheel contact band, accompanied by a dark spot containing cracks with a circular arc or V shape (Figure 32).

The cracks propagate inside the head, at first at a shallow angle to the surface. Then, when they reach 3 to 5 mm depth, they propagate downward transversely, producing the fracture of the rail.

This defect is often found on flash and aluminothermic welds, also in corrugated zones.

Squats on rails are located randomly and appear numerous, making them dangerous because of the risk of multiple fractures with significant gaps.

This morphology can be found locally or periodically on the gauge corner of high rails of curves, in zones with Head Checking.

Conventional means of detection:

- Visual inspection
- Ultrasonic testing

Recommendations for maintenance:

- Keep rail under inspection
- Removal of rails showing defects prejudicial to the safety of running contact
- Removal of broken rail

Maintenance strategies:

Surface initiated cracks can be effectively controlled when the shape of the railhead profile matches the prevailing wheel profiles and when the fatigued rail surface is regularly removed at appropriate intervals.

Reprofiling shall always be carried out as soon as possible after re-railing in order to optimize the condition of the rail surface (removal of decarburized layer, removal of damages from the

installation process, straightness at welds, etc.) and the target profile (wheel-adapted or AHC profiles).

In order to assure a long rail service life and consequently low LCC, the consecutive reprofiling cycles need to be programmed from the data of rail installation or a corrective reprofiling action respectively, taking into account the installed steel grades and other parameters as traffic load.

Shorter reprofiling intervals result in smaller metal removal requirements. Consequently, in such short periods, the development of surface-initiated cracks is limited.

The best strategy is preventive cyclic reprofiling with small metal removal requirements. Applying profiles with moderate gauge corner relief. Provided the interval between reprofiling cycles is appropriately matched with the initiation and subsequent growth of cracks, metal removal can be adjusted for one – pass regime, which is operationally the best option.

In order to maintain sections with a high sensitivity to surface-initiated cracks economically, a certain damage level can be accepted (as intervention threshold or as remaining depth after treatment).

However, this level needs to be kept small enough to be removed in a short time and not to interfere with safety issues.

The reprofiling interval and the related average metal removal should depend on actual measurements, which need to be checked again during reprofiling work. Such a policy optimizes the magnitude of artificial wear by reprofiling and hence prolongs rail life.

5.2 Description of Inputs

The following sections describe the physical parameters that are characteristic for the assets under investigation and the signal that are measured with the on-board monitoring system.

5.2.1 Physical Parameters

The following sections describe the physical parameters used as rail quality indicators.

5.2.1.1 Longitudinal Level

The longitudinal level is the standard physical parameter to assess vertical track irregularities. According to EN 13231-1 [22] and EN 13231-3 [23], four different wavelengths are of interest. They can be associated with different track defects [24]:

- 10 – 30 mm: surface defects of the rail head and rail joints
- 30 – 100 mm: surface defects of rail head, rail joints, rail wear caused by braking and short-pitch corrugation
- 100 – 300 mm: long-pitch corrugation (inner rail in curves)
- 300 – 1000 mm: rail defects persisting from the production of rails

According to this classification, the first two wavebands comprise the critical wavelength for the failure modes under investigation in this project.

The longitudinal level is normally measured with a hand-held measurement trolley.

5.2.1.2 Rail Surface Roughness

The microscale rail surface roughness comprises random non-periodic low-amplitude rail surface undulations that are smaller than the wheel-rail contact patch. Therefore, the wavenumber spectrum of these defects is very broad. The rail surface roughness increases the overall rail and wheel vibrations and hence the noise emissions.

5.2.2 Measured Signals

The SIA_ABA on-board sensor system is described in detail in Deliverable D4.1. The system measures the vertical, longitudinal and lateral acceleration at the axle-box. The failure modes investigated in this project according to the use cases specified in Deliverable D2.1 can be considered as vertical defects. Therefore, the vertical component of the ABA data is the most important with regards to defect detection and monitoring.

5.3 Description of Health Assessment Methodology

In order to relate the measured signals with the physical parameters indicating the rail health status, the ABA data needs to be processed and characteristic features extracted. Data analysis strategies for track condition monitoring using in-service vehicle dynamic measurements can be categorised in model-based and signal-based methods. Model-based methods provide a mathematical description of physical models. In this way, when a train passes a track defect with a given wavelength λ at a certain speed V , it experiments a vertical movement with a specific frequency f [25], which can be calculated as follows

$$f = V/\lambda \quad (35)$$

The simplest model relates the measured ABA data with the vertical movement and hence the longitudinal level of the track by double integration. This approach provides reliable results for track geometry defects with a wavelength of several meters. But this approach typically fails when small wavelength defects are examined. In this case, more complex models are necessary that also account for the non-linear vehicle-track interaction. With the complexity of the models, the number of model parameters increase. Those not only introduce a higher level of uncertainty but also increase computational costs. Therefore, parameter fitting by means of inverse modelling is limited. In contrast, signal-based methods purely rely on signal processing methodologies.

Here, the ABA signal time series are processed as shown in Figure 32. First, a Short-time Fourier transform (STFT) is applied to batches of the ABA time series. The STFT process breaks the input into smaller frames, which are then Fourier transformed. The STFT is a common time-frequency representation in vibration signal analysis. In order to separate the background noise from the signal generated by the wheel defects, the logarithmic amplitude spectrum is taken from the STFT. The background noise is generated by the vibrations excited by the wheel and rail roughness. Its logarithmic amplitude spectrum can be modelled as a scaled version of the logarithmic amplitude

spectrum of the average frequency response received at the accelerometer. The time-variant amplitude scaling depends on the train speed and is found through linear regression. Following the removal of the background noise, the logarithmic time-frequency representation is transformed into a distance-wavenumber representation. In this domain, the feature extraction takes place by computing the root mean square (RMS) amplitude of different wavelengths' ranges.

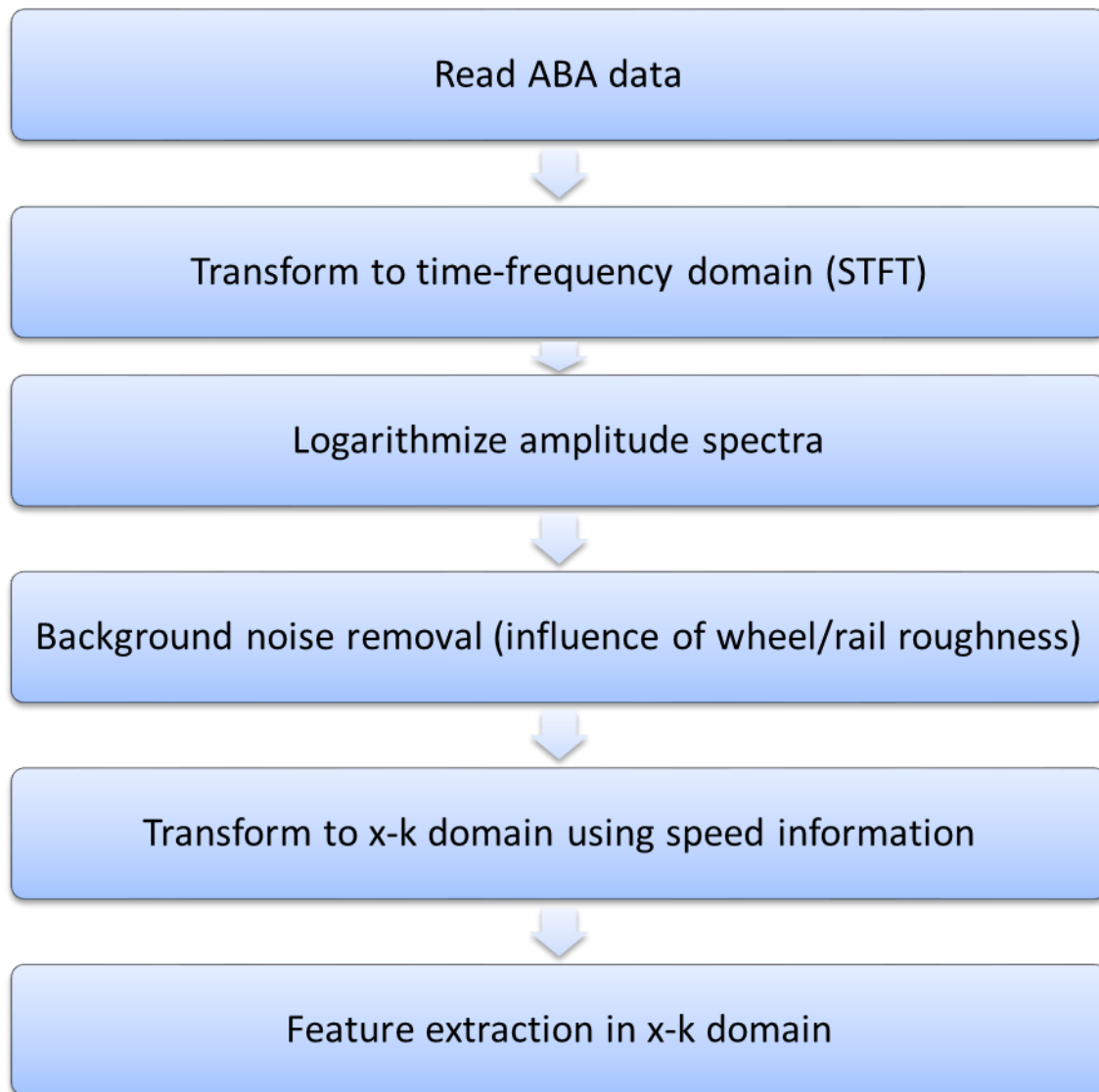


Figure 32. ABA data processing sequence to extract characteristic features for the rail health status assessment.

5.4 Results and Conclusions

In this section, the results of the signal processing and feature extraction sequence shown in Figure 32 are presented. The sequence was applied to a representative ABA data time series shown in Figure 33.

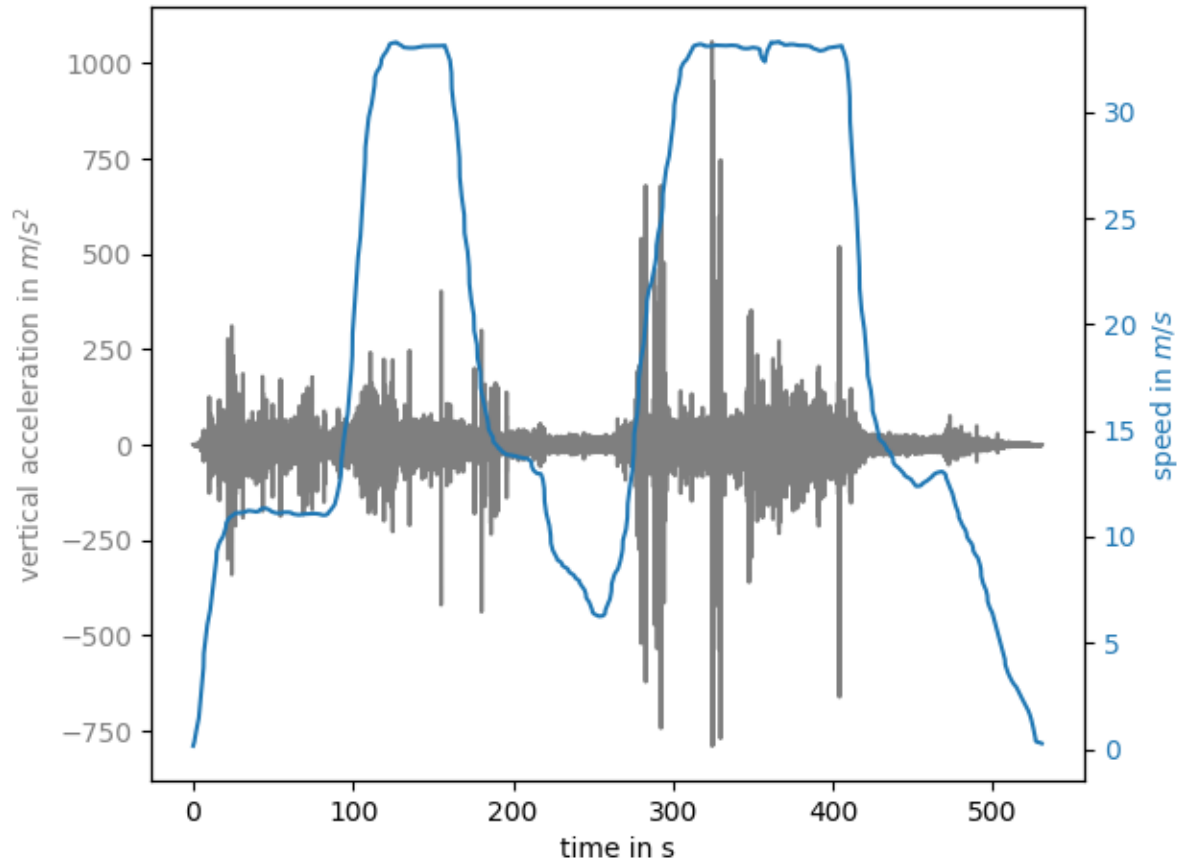


Figure 33. Raw ABA data in the time domain (grey) and GNSS speed (blue).

Distinctive peaks are visible in the raw data as well as in the time-frequency representation (Figure 34). Isolated track irregularities appear as vertical lines in the time-frequency representation (e.g. at approximately 40 s). The horizontal bands in the time-frequency representation represent the natural frequencies (and their harmonics) of the track and the vehicle. Those frequencies are permanently excited due to the roughness of the rail and the wheel. The frequency bands are removed before feature extraction (see Figure 32).

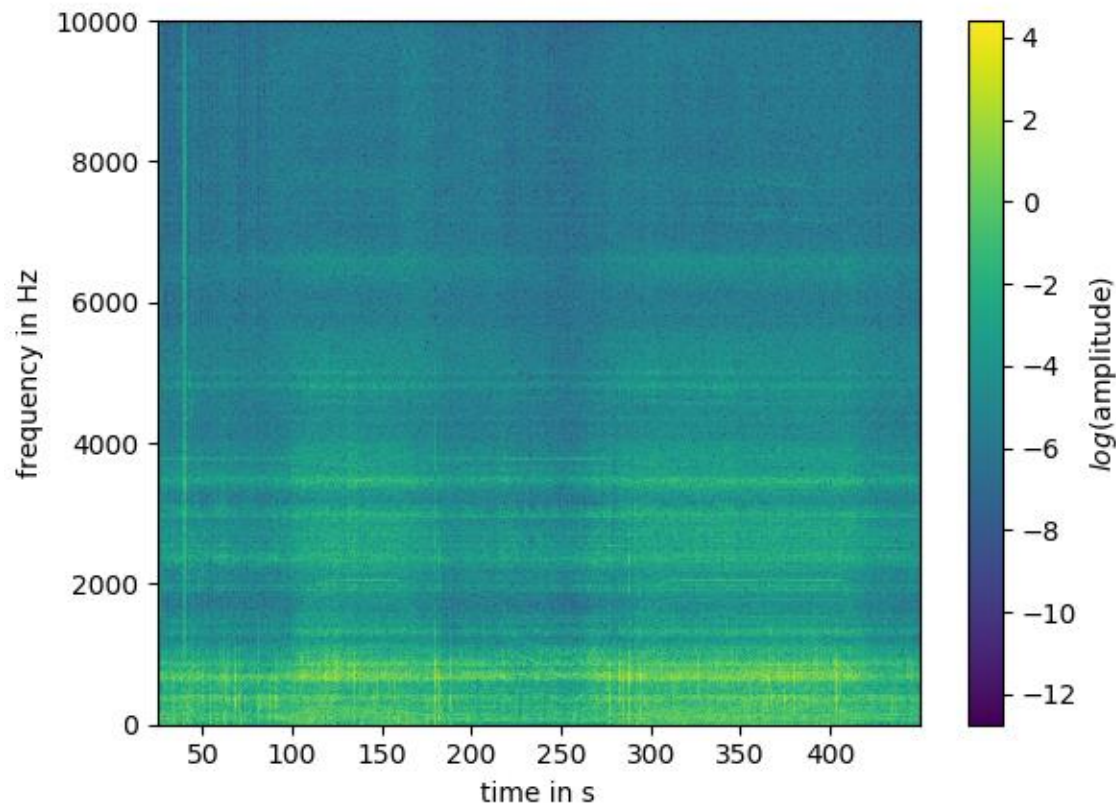


Figure 34. Time-frequency representation of raw ABA data.

The extracted features show that the observed track irregularities are characterised by different wavenumber ranges (the wavenumber is the reciprocal of the wavelength). For instance, the peak at ca. 166 m (corresponding to the peak at 40 s in the time-frequency domain) has the highest amplitude in the wavenumber band 149 – 300 1/m (3.33 mm – 6.71 mm wavelength). In contrast, the peak at 8258 m has its highest amplitude at wavenumber band 9 – 18 1/m (55.56 mm – 111.11 mm wavelength). According to the classification made in section 5.2.1.1, the first track irregularity could be attributed to an isolated railhead defect (e.g. small squat) while the second irregularity could indicate short-pitch corrugation. Since there is no reference data available for this track segment, this assumption cannot be verified. However, due to the fact that most defects in this wavelength range are corrected by rail grinding, a wrong defect classification, in this case, would not have a negative impact on the planning of the maintenance activity. Furthermore, if a track irregularity at a defined position is monitored using data from several journeys, the repeatability of the results can be used as validation and probability measure of the defect classification.

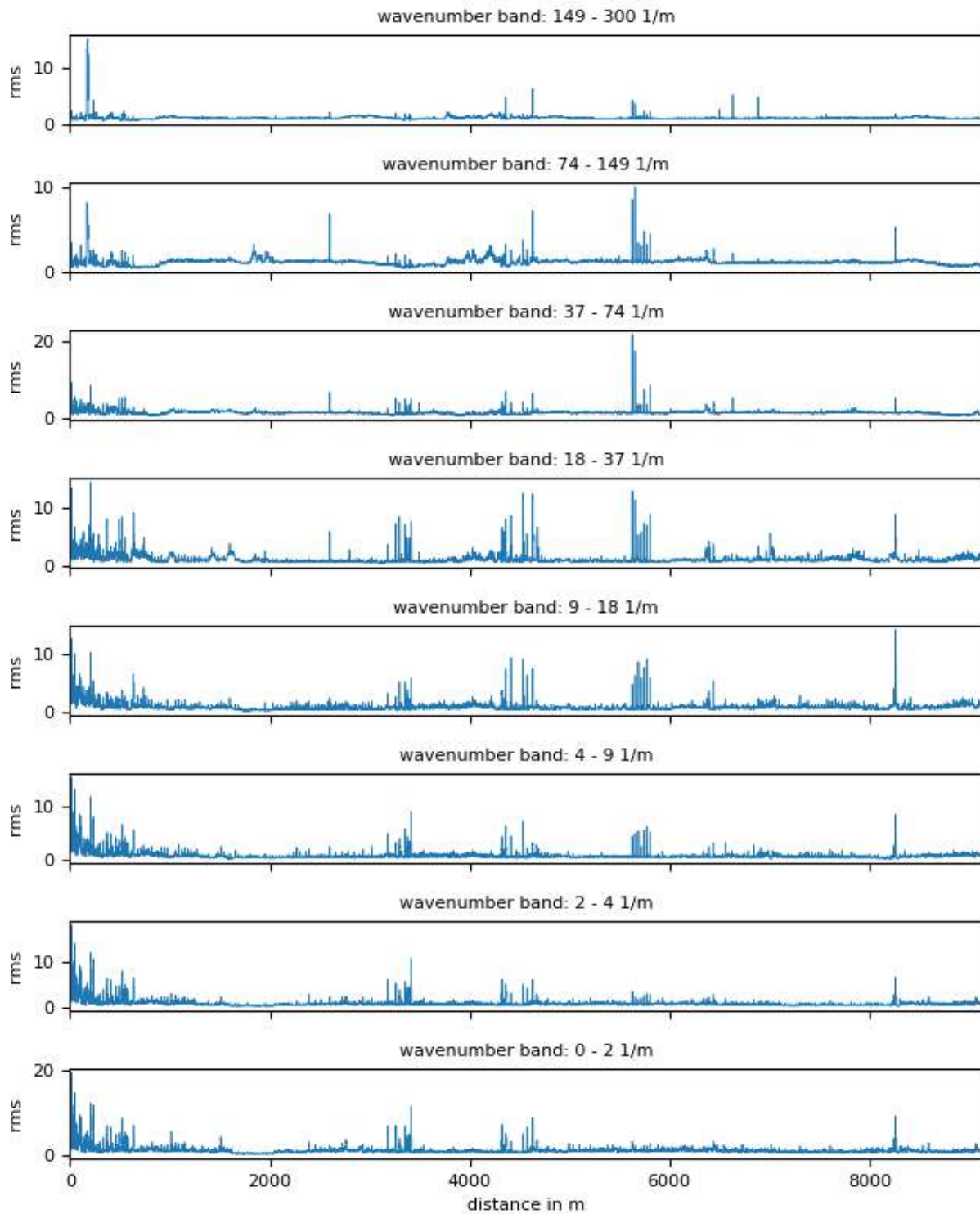


Figure 35. RMS features from eight different wavenumber bands.

5.4.1 The Impact of E-GNSS

For the assessment of the health status of the rail based on the methodology described in 5.3 an accurate estimation of the train speed is required, which is necessary to convert the measured frequencies to wavelength. This is crucial for the classification of track defects (see section 5.2.1.1). Furthermore, precise absolute and relative positioning is necessary to locate track defects on the track and to measure the relative distance between irregularities to link them to e.g. joins of track segments, respectively.

In SIA deliverable D3.2 [26] the benefits of E-GNSS are exploited. It was shown that the use of E-GNSS increases the number of visible satellites in the challenging rail environment. This effect is reflected in an increased satellite count when a higher elevation mask is applied and in the dilution of precision (DOP) parameters, which relate to the quality of the best obtainable positioning solution. Since the amplitude of the ABA data is linearly dependent on vehicle speed, increasing the accuracy of the speed estimate by 1% also improves the estimate of the severity of a track fault by 1%.

Incorporating E-GNSS therefore directly correlates to the success of the track monitoring and track health status assessment.

6 References

- [1] ISO 1005-8. Railway rolling stock material — Part 8: Solid wheels for tractive and trailing stock — Dimensional and balancing requirements
- [2] EN50405. Railway applications. Current collection systems. Pantographs, testing methods for contact strips
- [3] EN50119. Railway applications - Fixed installations - Electric traction overhead contact lines
- [4] D2.1. SIA deliverable: End user requirements of SIA and validation plan (v5.0)
- [5] D4.1. SIA deliverable: Wheel to rail and pantograph to catenary sensing nodes (v4.0)
- [6] D4.3. SIA deliverable: On-board data integration platform and train-track communication hub (v4.0)
- [7] S. Bruni et al., "The results of the pantograph – catenary interaction benchmark," *Veh. Syst. Dyn.*, vol. 53, no. 3, pp. 412–435, 2015.
- [8] EN50367. Railway applications - Current collection systems - Technical criteria for the interaction between pantograph and overhead line (to achieve free access)
- [9] CA-220 catenary. ADIF: Catenary CA-160 and CA-220 description
- [10] S. Gregori, M. Tur, E. Nadal, J. V. Aguado, F. J. Fuenmayor, and F. Chinesta, "Fast simulation of the pantograph–catenary dynamic interaction," *Finite Elem. Anal. Des.*, vol. 129, no. September 2016, pp. 1–13, 2017.
- [11] EN50318. Railway applications - Current collection systems - Validation of simulation of the dynamic interaction between pantograph and overhead contact line
- [12] S. Gregori, M. Tur, A. Pedrosa, and F. J. Fuenmayor, "The Use of Bayesian Optimisation Techniques for the Pantograph-Catenary Dynamic Interaction Stochastic Problem," *EngOpt 2018 Proc. 6th Int. Conf. Eng. Optim.*, pp. 997–1008, 2019.
- [13] O. V. Van, J. P. Massat, C. Laurent, and E. Balmes, "Introduction of variability into pantograph-catenary dynamic simulations," *Veh. Syst. Dyn.*, vol. 52, no. 10, pp. 1254–1269, 2014.
- [14] G. Bucca and A. Collina, "Electromechanical interaction between carbon-based pantograph strip and copper contact wire: A heuristic wear model," *Tribol. Int.*, vol. 92, pp. 47–56, 2015.
- [15] A. Bracciali and G. Cascini, "Detection of corrugation and wheel flats of railway wheels using energy and cepstrum analysis of rail acceleration," *Proceedings of the Institution of Mechanical Engineers, Part F: Journal of Rail and Rapid Transit*, vol. 211, no. 2, pp. 109–116, 1997.
- [16] M. Meywerk, "Polygonalization of Railway Wheels," *Archive of Applied Mechanics (Ingenieur Archiv)*, vol. 69, no. 2, pp. 105–120, 1999.

- [17] Nielsen, J. C. O. and A. Johansson, "Out-of-round railway wheels-a literature survey," *Proceedings of the Institution of Mechanical Engineers, Part F: Journal of Rail and Rapid Transit*, vol. 214, no. 2, pp. 79–91, 2000
- [18] A. Johansson and C. Andersson, "Out-of-round railway wheels—a study of wheel polygonalization through simulation of three-dimensional wheel–rail interaction and wear," *VEHICLE SYSTEM DYNAMICS*, vol. 43, no. 8, pp. 539–559, 2005.
- [19] G. Pallgen, "Unrunde Räder an Eisenbahnfahrzeugen: Durch ortsfeste Meßanlagen können unrunde Räder an Schienenfahrzeugen detektiert werden," *EI*, vol. 1, no. 49, pp. 56–60, 1998.
- [20] F. Braghin, R. Lewis, R. S. Dwyer-Joyce, and S. Bruni, "A mathematical model to predict railway wheel profile evolution due to wear," *Wear*, vol. 261, no. 11-12, pp. 1253–1264, 2006.
- [21] *DIN EN 15313:2016-09, Bahnanwendungen - Radsätze und Drehgestelle - Radsatzinstandhaltung; Deutsche Fassung EN 15313:2016*, 2016.
- [22] EN13231-1. Railway applications - Track - Acceptance of works - Part 1: Works on ballasted track - Plain line, switches and crossings
- [23] EN13231-3. Railway applications - Track - Acceptance of works - Part 3: Acceptance of reprofiling rails in track
- [24] J. Valehrach, P. Guziur, T. Riha, and O. Plasek, "Assessment of rail long-pitch corrugation," *IOP Conf. Ser.: Mater. Sci. Eng.*, vol. 236, p. 012048, 2017.
- [25] P. Salvador, V. Naranjo, R. Insa, and P. Teixeira, "Axlebox accelerations: Their acquisition and time–frequency characterisation for railway track monitoring purposes," *Measurement*, vol. 82, pp. 301–312, 2016.
- [26] D3.2. SIA deliverable: Positioning algorithms based on multisensory inputs (v4.0)